Applied Geochemistry 191 (2025) 106494

Contents lists available at ScienceDirect

Applied Geochemistry

journal homepage: www.elsevier.com/locate/apgeochem

Trace element compositions and redox shifts preserved in magnesites, sediments and soils from the Kunwarara magnesite mine

Carl Swindle [a,d,*], Paulo Vasconcelos [b], Nathan Dalleska [a], Emily Cardarelli [c,e], Surjyendu Bhattacharjee [a], Zoe Dimarco [b], Kenneth A. Farley [a], Theodore Present [a]

[a] Division of Geological and Planetary Sciences, California Institute of Technology, Pasadena, CA, 91125, United States of America
[b] School of Earth and Environment Sciences, The University of Queensland, Brisbane, Queensland, 4072, Australia
[c] NASA Jet Propulsion Laboratory, California Institute of Technology, Pasadena, CA, 91109, United States of America
[d] The B. John Garrick Institute for the Risk Sciences, University of California, Los Angeles, CA, 90095, United States of America
[e] Department of Earth, Planetary and Space Sciences, University of California, Los Angeles, CA, 90095, United States of America

ARTICLE INFO

Keywords:
Magnesite
Rare Earth elements
Redox sensitive elements
Cerium anomaly
Redox conditions

ABSTRACT

Magnesium carbonates in surficial environments act as CO_2 sinks and can record aspects of the palaeohydrological cycles on Earth and Mars. In natural environments, magnesium carbonates can be intimately intermixed at the micrometer scale with complex assemblages of other non-carbonate minerals. To better determine magnesium carbonate composition in complex samples and minimize contamination from secondary Fe/Mn-oxides/hydroxides, we developed and assessed methods for sample cleaning, selective digestion, and quadrupole inductively coupled plasma mass spectrometry to measure the trace and minor elemental composition. By pre-cleaning and selectively digesting carbonate, we identified previously unrecognized geochemical trends in magnesite ± dolomite nodules and their host fluvial sediments collected along a depth profile at the Kunwarara magnesite mine, Queensland, Australia. In particular, Ce anomalies in magnesite diminishes with depth coincident with decreasing abundances of authigenic Fe/Mn-oxides/hydroxide minerals in the host sediments. These results reveal how the magnesium carbonates capture interactions between the ascending groundwaters and descending surface waters. We further demonstrate the value of magnesium carbonate-specific trace element data with reanalysis of previously published ion microprobe data from Martian meteorite ALH84001, which also shows Ce fractionation. Accurate mineral-specific trace and minor element measurements in Earth and Martian magnesium carbonate samples improve our understanding of the timing and identities of carbonate mineral-forming reactions that occurred on both planets.

1. Introduction

While magnesite is relatively uncommon on Earth, it has been detected by orbital and in situ observations on the Martian surface, notably at Jezero crater, which is the exploration site for the Mars 2020 Perseverance rover (Brown et al., 2020; Clavé et al., 2023; Ehlmann et al., 2008; Farley et al., 2022; Scheller et al., 2021, 2022; Stack et al., 2024). Trace element concentrations in carbonates place useful constraints on the hydrous fluid conditions (such as pH and Eh) in which the carbonates formed, thereby recording past environmental conditions (Y.-G. Liu et al., 1988; Möller, 1989; Smrzka et al., 2019; Zhao et al., 2022). Protocols that are utilized for determining trace element concentrations in Ca-carbonates (such as calcite and aragonite) by selectively digesting the carbonate have been assessed in detail (e.g., Boyle, 1981; Cao et al., 2020; Tostevin et al., 2016; Yu et al., 2005; Zhao et al., 2022). However, magnesium carbonates such as magnesite (trigonal $MgCO_3$) and dolomite (trigonal $CaMg(CO_3)_2$) are less soluble and their elemental compositions are generally determined by aggressive whole-rock digestions. Digestion protocols for solution inductively coupled plasma mass spectrometry (ICP-MS) analyses of magnesite have involved heated bulk digestions in mixtures of strong acids such as mixtures of concentrated nitric acid and hydrofluoric acid (e.g., Fernandez-Nieto et al., 2003; Kilias et al., 2006; Lugli et al., 2000) and concentrated nitric acid and hydrochloric acid (e.g., Dong et al., 2016; Kuşcu et al., 2017). Following implementation of heated concentrated nitric acid and hydrofluoric acid digestions, Fernandez-Nieto et al.

---

[*] Corresponding author. Division of Geological and Planetary Sciences, California Institute of Technology, Pasadena, CA, 91125, United States of America.
E-mail address: cswindle@risksciences.ucla.edu (C. Swindle).

https://doi.org/10.1016/j.apgeochem.2025.106494
Received 23 October 2024; Received in revised form 22 June 2025; Accepted 6 July 2025

(2003) and Lugli et al. (2000) found that Rare Earth Element (REE) concentrations and those of other trace elements (e.g., Rb, Cs, Ga, Zr, Th, V, and Sc in Lugli et al., 2000) were positively correlated with Si and Al concentrations in the magnesites. They concluded that the reported values of many trace element concentrations were largely controlled by the presence of co-existing detrital aluminosilicate phases. Similarly, heated digestions in concentrated nitric acid and hydrochloric acid implemented by Dong et al. (2016) and Kuşcu et al. (2017) would not be expected to dissolve most silicate minerals, but these strong, oxidizing acids still may attack iron oxides, water-soluble salts, phyllosilicates, and trace elements adsorbed onto grain surfaces, introducing trace and minor elements not present in the carbonate into the analytical solution (Cao et al., 2020).

To avoid such contamination, others have attempted physical separation of non-carbonate phases prior to digestion (e.g., Henjes-Kunst et al., 2014; Mervine et al., 2015). Large contaminant grains may be removed by hand picking or density and magnetic separation, though separating fine-grained contaminants or elements adsorbed to mineral surfaces may be impossible (e.g., Mervine et al., 2015).

Mg-carbonate specific trace element concentrations can be determined on grains that are visibly free of contaminant grains by laser ablation inductively coupled plasma mass spectrometry (LA-ICP-MS) and secondary ion mass spectrometry (SIMS) (e.g., Eiler et al., 2002; Lu et al., 2022). These methods may be appropriate for measuring concentrations of trace elements in sufficiently large Mg-carbonate grains. However, such analyses may not adequately represent trace element characteristics of bulk carbonate at a larger scale. Accuracy and precision of microanalytical methods across a broad range of trace and minor elements is also challenging due to complicating effects of material properties like porosity or grain orientation (Pittman, 1971; Isa et al., 2017; Marin Carbonne et al., 2022), which are commonly variable in and among fine crystalline carbonates.

X-ray fluorescence (XRF) has also been used to determine trace element contents of magnesites, though this approach is also susceptible to contributions from non-carbonate inclusions. Silicate inclusions can introduce as much as 10 wt % SiO_2 to carbonate analyses (e.g., Oskierski et al., 2013). While XRF mapping has the spatial resolution to identify some contaminants, accuracy is also subject to a variety of factors, such as porosity and purity. Magnesite bearing trace elements have also been determined by neutron-activation analysis (NAA). As with XRF, this method analyzes non-carbonate impurities (Croudace et al., 1982; Greenberg et al., 2011).

Here, we modified a leaching and digestion protocol developed to selectively determine trace element concentrations in calcite by Cao et al. (2020) to dissolve magnesite and dolomite samples by heating the acid. Samples were analyzed by solution quadrupole ICP-MS, and elemental concentrations in the carbonates were determined by calibration to matrix-matched (magnesium-enriched) multi-element standards.

To assess the protocol's efficacy for selectively digesting Mg-carbonates, we compare elemental concentrations and derived products, such as Ce anomaly (Ce*), determined by this procedure with those determined by heated 5 % nitric acid digestion for several magnesite with dolomite samples collected from an open pit mine in Kunwarara, Queensland, Australia. Magnesite and dolomite nodules were sampled along a depth profile in the Kunwarara magnesite mine, where these Mg-carbonate nodules and cements formed by replacement of detrital fluvial sediments that were altered by pedogenic processes, and are intimately associated with authigenic phyllosilicates, oxides, and silica phases (Milburn and Wilcock, 1994, 1998; Searston, 1998). The value of such results is further demonstrated with a reanalysis of trace metal data from magnesium carbonates in Martian meteorite ALH84001 from (Eiler et al., 2002).

2. Materials and methods

2.1. Geologic background

Mg-carbonates (magnesite ± dolomite) and host sediments analyzed in this study were collected from the Qmag magnesite mine in Kunwarara, Marlborough, Queensland, Australia from exposures in a fresh pit mine wall. The pit, which was excavated into soil and unlithified fluvial sediments, exposed various types of Mg-carbonates (pure magnesite and magnesite + dolomite) (Milburn and Wilcock, 1994, 1998; Searston, 1998; Wilcock, 2000).

The Kunwarara deposit is one of the largest cryptocrystalline magnesite deposits in the world, and hosts an estimated 500 million tons of magnesite reserves (Searston, 1998). Mining has exposed the magnesite hosted in post-Eocene to Quaternary age fluvial sediments and soils situated along the upper tributaries of the Herbert Creek catchment (Milburn and Wilcock, 1994, 1998; Pope, 2007; Searston, 1998; Wilcock, 2000). The mine is situated in a sedimentary basin that is defined by low relief hills comprised of granitoids, metasediments and serpentinites (Searston, 1998). The fluvial sequence is up to 46 m thick, and generally fines up from gravel or coarse sand at the base of the sequence to fine sand, silt, and mud near the surface (Milburn and Wilcock, 1994, 1998; Searston, 1998; Wilcock, 2000). Minerals largely consist of feldspars, quartz grains, and clay minerals with minor oxides (Searston, 1998) and magnesite is restricted to the upper half (~4–16 m) of the sediments, excluding a surficial (~1–7 m) layer of clay-rich soil (Milburn and Wilcock, 1998). Milburn and Wilcock (1998) described the texture of nodular magnesites from Kunwarara as cryptocrystalline and creamy-white to pure white in color with carbonate crystals ranging between 1 and 10 μm in size forming as: 1) nodules of several millimeters to 60 cm in diameter; 2) intergrown veins and sheets; or 3) cemented aggregates that are up to 1 m in diameter. The magnesites vary between hard, pure, and porcelaneous samples with a conchoidal fracture to softer, porous, and chalky varieties. Non-carbonate minerals closely associated with the magnesites include amorphous silica, clays, pyrite, and iron and manganese oxides. Searston (1998) noted that the less dense, softer, porous, and chalky magnesites more often host inclusions of these extraneous minerals.

2.2. Sample descriptions and selection

Four carbonate samples and five samples of host sediment were collected along a depth transect exposed in the Kunwarara mine, and an additional magnesite nodule was collected from nearby (Fig. 2, Table 1). Paired host sediment samples for magnesites K-7.6, K-9.8 and K-10.8 were collected less than 10 cm away from the co-existing carbonates and are denoted with an S at the end of the same sample name (Table 1). An additional sediment sample (K-3.4S) was collected from the uppermost horizon that lacked carbonate (0–6.8 M depth). At the 8.3–9.3 m depth range, a magnesite + dolomite sample (K-8.8) and its associated host sediment (K-8.8S) were collected, but only the host sediment was analyzed due to the heterogeneity of the carbonate at the hand sample scale (~1–10 cm). One carbonate sample of exceptional mineralogical purity (K-10.8) was tested against a sample with mineralogical complexity (K-7.6 – trace Fe/Mn-oxide/hydroxides – no silicates) to test the efficacy of the carbonate mineral-selective digestion described in Section 2.3 (Fig. 1, Table 1). These carbonate samples were split into several aliquots to compare the selective digestion method with a 5 % nitric acid digestion heated to 90 °C. All other carbonate samples from Kunwarara were analyzed only by the selective digestion method.

Magnesite sample M22-224E was used as a baseline for assessing ICP-MS analysis accuracy for Mg-rich solutions with matrix compositions similar to samples. It was collected from the Old Man South pit of the Kunwarara mine and is the outer edge of a ~5 cm diameter magnesite nodule. The solution resulting from carbonate mineral-selective digestion served as a spike-free initial solution used for a

Table 1
Metadata associated with analyzed samples from the Kunwarara magnesite mine. Sed stands for sediments, Mgs stands for magnesite, Dol stands for dolomite, Fe/Mn–O stands for Fe/Mn-oxides/hydroxides, and Si–O–Al stands for aluminosilicates. The depth in meters is measured relative to the surface.

Sample Name	Field Label	Rock Type	Depth (m)	Description	Texture
K-3.4S	19-AUS-20S	Sed	0–6.8	Si–*O*–Al, Fe/Mn–O, Clay	Brittle
K-7.6	19-AUS-19	Mgs + Dol	6.8–8.3	Mgs + Dol Nodule	Soft
K-7.6S	19-AUS-19S	Sed	6.8–8.3	Si–*O*–Al, Fe/Mn–O, Clay	Brittle
K-8.8S	19-AUS-24S	Sed	8.3–9.3	Si–*O*–Al, Fe/Mn–O, Clay	Brittle
K-9.8	19-AUS-23	Mgs	9.3–10.3	Mgs Nodule	Hard
K-9.8S	19-AUS-23S	Sed	9.3–10.3	Si–*O*–Al, Fe/Mn–O, Clay	Brittle
K-10.8	19-AUS-22	Mgs	10.3–11.3	Mgs Nodule	Hard
K-10.8S	19-AUS-22S	Sed	10.3–11.3	Si–*O*–Al, Clay	Brittle
K-11.8	19-AUS-21	Mgs	11.3–12.3	Mgs Nodule	Hard
M22-224E	M22-224E	Mgs	7.3	Mgs Nodule	Hard

recovery test of the trace elements measured in these samples.

Analyzing a high-purity magnesite geochemical reference material with certified concentrations of the trace elements of interest would have been ideal, but, to our knowledge, no such well-characterized material exists. Instead, a dolomitic reference material (DWA-1, produced by Liege University and distributed by Brammer Standards, Inc.) was analyzed to ensure that the procedures used in this study produce data that is consistent with recommended and proposed concentrations (Roelandts and Duchesne, 1994).

2.3. Leaching and hot acetic acid digestion

Aliquots of Mg-carbonate powders were produced by gently abrading carbonate fragments from a sample or using a diamond-studded high-speed rotary drill to extract powder from samples. The abraded or drilled fragments were powdered lightly and homogenized with an agate mortar and pestle. Aliquots (~4.5–9 mg) of the powders were weighed into 1.5 ml polypropylene centrifuge tubes (K-7.6: 8 aliquots, K-10.8: 2 aliquots, K-9.8: 1 aliquot, K-11.8: 1 aliquot, M22-224E: 1 aliquot; and DWA-1: 3 aliquots). Sample batches were processed with three to four procedural blanks (Table A1).

Methods for cleaning and dissolving magnesite samples for trace and minor element analysis were modified from Cao et al. (2020). Carbonates were pre-cleaned in ammonium acetate and Milli-Q water and then digested in heated acetic acid. The insoluble residue was filtered (apparently quartz and opaque oxides), and the liquid fraction was analyzed by solution ICP-MS. Magnesite is less soluble in weak acid than other carbonates, so we digested samples in heated acetic acid rather than at room temperature as done by Cao et al. (2020). The sample leaching and digestion protocol is schematically summarized in Fig. 3. Samples were leached twice in 1.5 mL of 1.0 M ammonium acetate solution to dissolve water-soluble salts and remove adsorbed ions on grain surfaces by ion exchange with excess NH^{4+} ions. Ammonium acetate solution of pH 7 was prepared from anhydrous ammonium acetate (BioUltra Fluka Analytical) in 18.2 MΩ-cm ultrapure water (Millipore Milli-Q).

Tubes containing the carbonate powder samples with ammonium acetate were shaken vigorously by hand to disperse the sample throughout the solution, sonicated for 15 min, shaken vigorously again, sonicated again for 15 more minutes, and shaken vigorously once more. Samples were centrifuged at 13,200 RPM for 10 min and the ammonium acetate solution was decanted away with a pipette. These steps were repeated twice. Neutral ammonium acetate rinses introduce an excessive amount of ammonium ions to the samples, which substitutes for trace elements adsorbed to grain surfaces (Cao et al., 2020). These rinses also remove water-soluble salts (e.g., NaCl or gypsum) associated with the carbonate samples. Following the ammonium acetate rinses, samples were subsequently rinsed in 1.5 mL ultrapure Milli-Q water, shaken, and centrifuged at 13,200 RPM for 10 min before pipetting and discarding the supernatant. Three consecutive Milli-Q rinses ensured the removal of trace elements adsorbed to grain surfaces or present in water-soluble salts.

Following these rinses, samples were resuspended in 1.5 mL of 0.3 M acetic acid (Cao et al., 2020), shaken, and poured into labeled 50 mL polypropylene DigiTUBEs sourced from SCP SCIENCE. The original

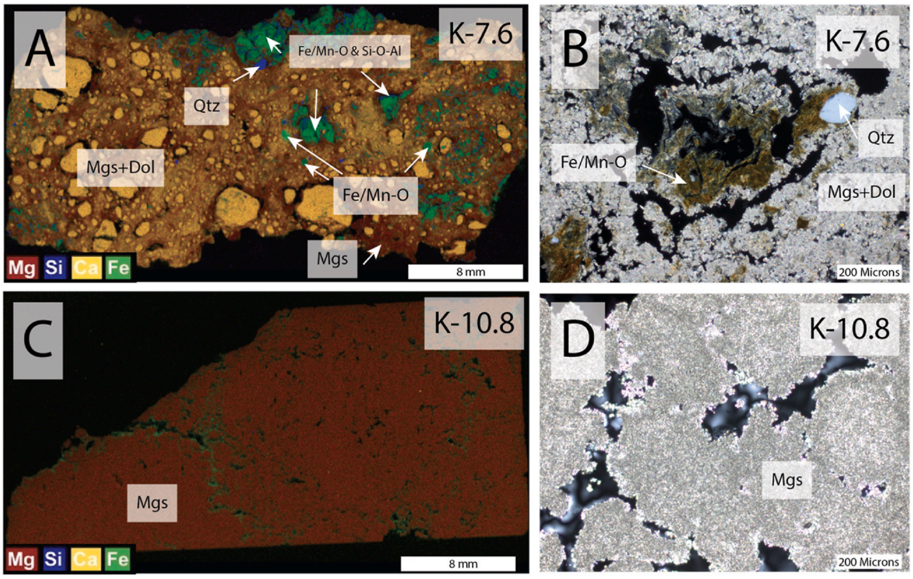

Fig. 1. Representative micro-XRF (x-ray fluorescence) images (A&C) and optical images of thin sections taken in cross polarized light (B&D) of K-7.6 (A–B) and K-10.8 (C–D). We use the following abbreviations: Magnesite (Mgs), dolomite (Dol), Fe/Mn-oxides/hydroxides (Fe/Mn–O), aluminosilicates (Si–*O*–Al), and quartz (Qtz).

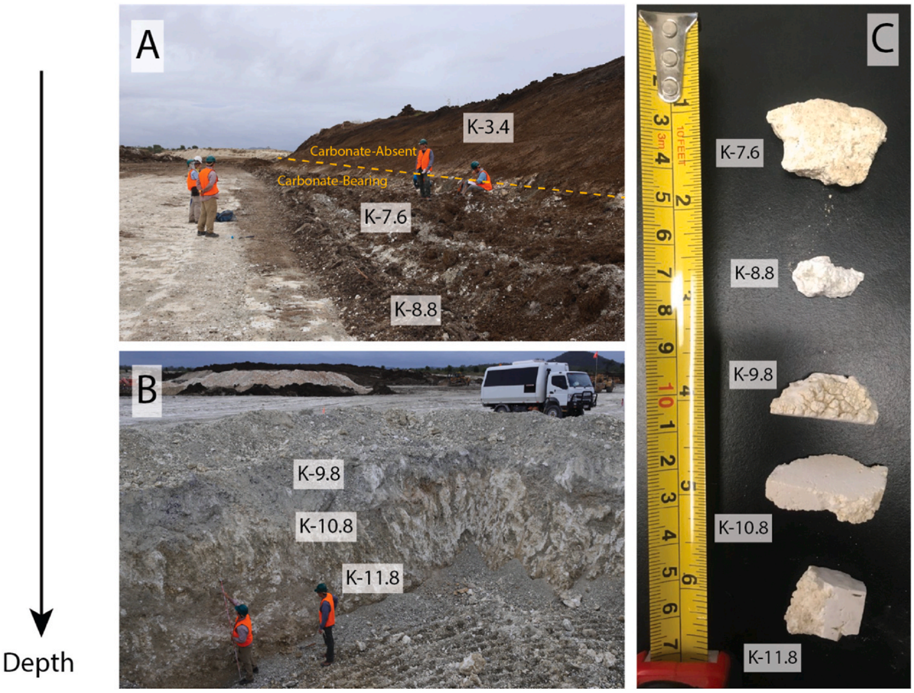

Fig. 2. Depth transect at Kunwarara (Panels A and B) and photographs of portions of the Mg-carbonate nodules collected along the depth profile (Panel C). True depth ranges at which samples were collected are available in Table 1. The base of the pit in Panel A is at equivalent depth to the surface of the pit in Panel B. No carbonate was sampled at K-3.4 (only a sediment sample K-3.4S).

centrifuge tubes were rinsed twice more with 1 mL of 0.3 M acetic acid that was shaken and poured into the DigiTUBEs to ensure complete transfer (>99 %) of the samples. The DigiTUBEs were capped and heated to 90 °C for 1–2 h until completely dissolved and then cooled to near room temperature. At these conditions, the dissolution rates of magnesite can be orders of magnitude faster than clay and metal-oxide phases (Cama et al., 2002; Pokrovsky et al., 2009; Saldi et al., 2010; White et al., 1994). The solutions were filtered directly into new DigiTUBEs with 0.2-μm hydrophilic polyethersulfone membrane syringe filters (Thermo Scientific) that were pre-rinsed with 0.3 M acetic acid; this step removes insoluble residual materials (e.g., silicates and oxides). Prior to drying, 6.5 mL of 5 % nitric acid was added to the samples to oxidize acetate in solution while drying. The samples in the DigiTUBEs with caps removed were dried down completely on a 90 °C hot-block. Digests were then resuspended in 50 mL of 5 % distilled nitric acid and left stored in capped DigiTUBEs for >12 h at room temperature. Immediately prior to ICP-MS trace element analysis, samples were well shaken by hand in the DigiTUBEs to ensure that the solutions were well mixed.

2.4. Heated nitric acid digests

Aliquots of carbonate samples K-7.6 (8 aliquots), K-10.8 (2 aliquots), and DWA-1 (3 aliquots) were also digested in 5 % distilled nitric acid that dissolves Fe/Mn-oxides/hydroxides. Three or more procedural blanks were processed and analyzed with each batch of samples. Carbonate powder aliquots were weighed into 1.5 mL polypropylene centrifuge tubes to which 1.5 mL of 5 % nitric acid was added. The tubes were sonicated for 15 min, shaken by hand, and vented for approximately 5 s to release pressure build up from CO_2. The steps involving sonicating, shaking, and venting were repeated twice. Samples were then poured into DigiTUBEs. Centrifuge tubes were rinsed with 1 mL 5 % nitric acid twice and poured into the DigiTUBEs, ensuring complete sample transfer. The samples were then digested in capped DigiTUBEs on a hot block at 90 °C for 1–2 h. Solutions were filtered directly into new DigiTUBEs using 0.2-μm hydrophilic polyethersulfone membrane syringe filters that were pre-cleaned with 5 % nitric acid. Solutions were dried down completely in DigiTUBEs at 90 °C for ~3–6 h and were then brought up to 50 mL in 5 % distilled nitric acid. Samples were left stored in capped DigiTUBEs for >12 h and shaken by hand prior to ICP-MS analysis to ensure that solutions were well-mixed.

2.5. Cold concentrated nitric acid digestion

To validate accuracy, four ~4.5–7.5 mg aliquots of the dolomite certified reference material DWA-1 were digested with concentrated nitric acid. Aliquots were weighed into labeled DigiTUBEs along with five procedural blanks. 3 mL of concentrated 70 % distilled nitric acid were added to the DigiTUBEs and samples were left to dissolve while capped at room temperature for ~24 h. The samples were then dried down for >24 h on a hot plate. Once all the nitric acid evaporated from the DigiTUBEs, samples and procedural blanks were brought up in 50 ml of 5 % distilled nitric acid. After sitting for >12 h, DigiTUBEs were shaken by hand prior ICP-MS analysis to ensure that solutions were well-mixed.

2.6. ICP-MS trace element standardization and matrix matching

Standard solutions were prepared in 5 % distilled nitric acid. Mg was sourced from Spec Pure from Alfa Aesar, 1000 micro-g/mL Stock # 385. REEs (La, Ce, Pr, Nd, Sm, Eu, Gd, Tb, Dy, Ho, Er, Tm, Yb, and Lu), Sc, Y, U, and Th were used to calibrate standard solutions were sourced from Inorganic Ventures CMS-1 (10 μg/ml). Sr used for standard solutions was sourced from MSSR-100PPM of Inorganic Ventures. Mo used for standard solutions was sourced from Fluka Analytical 04488-100 mL 1 ppm Mo. Ca used for standard solutions was sourced from BDH Aristar Plus 82025-960 1000 ppm Ca. Cd, Co, Cr, Cu, Fe, Mn, Ni, V, and Zn used for standard solutions were sourced from Specpure Transition Metals 44518 - 100 ppm.

A stock standard solution with the highest concentrations of trace elements contained 50,000 ppb Ca; 5000 ppb Sr; 500 ppb Cd, Co, Cr, Cu, Fe, Mn, Ni, V, and Zn; 50 ppb of REEs, Sc, Y, U, and Th; 1 ppb Mo. Five standards were produced with trace element concentrations equivalent

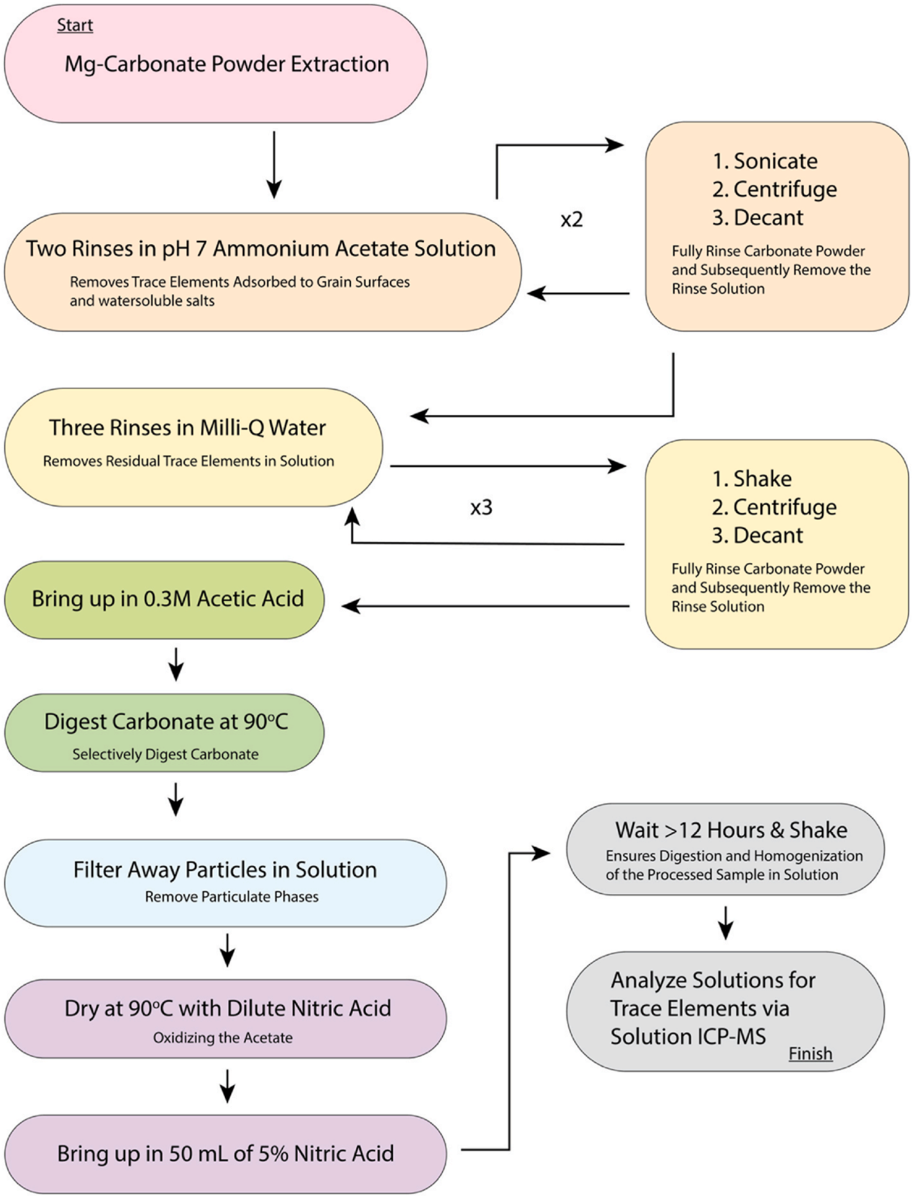

Fig. 3. Schematic workflow of the digestion protocol presented in this work modified from Cao et al. (2020) to be applied to magnesite ± dolomite. Further details are described in Sections 2.3, 2.6, and 2.7.

to 10x, 100x, 1,000x, 10,000x, and 100,000x dilutions of the stock standard solution in addition to an acid blank. When analyzing nearly pure magnesite samples (non-dolomitic), standards were matrix matched with 28.4 mg/L Mg to match the matrix of ~5 mg of magnesite dissolved in 50 mL of 5 % nitric acid. In addition to these matrix-matched trace element standards, a 14.2 mg/L Mg solution and a 2.84 mg/L Mg solution were produced to construct calibration curves for Mg.

Separate Mg- and Ca-concentration matched standards were used for analysis of the dolomitic samples K-7.6 and DWA-1, which matched the major element concentrations of 5 mg of material dissolved in 50 mL. The Ca/Mg was determined via ICP-MS prior to these analyses to ensure accurate matrix matching Mg and Ca were added. The standards for trace element calibration for K-7.6 contained 12.2 mg/L Ca and 20.0 mg/L Mg, and the standards for analysis of DWA-1 contained 21.7 mg/L Ca and 13.2 mg/L Mg. For each sample, a separate suite of major element standards was produced with concentrations equivalent to a 2x dilution of the Ca–Mg matrix and a 10x dilution of the Ca–Mg matrix to construct calibration curves for Ca and Mg in solution prepared from different powder aliquots of K-7.6 and DWA-1.

2.7. ICP-MS protocol and data reduction

The isotopes ^{24}Mg, ^{43}Ca, ^{45}Sc, ^{51}V, ^{52}Cr, ^{55}Mn, ^{56}Fe, ^{59}Co, ^{60}Ni, ^{63}Cu, ^{66}Zn, ^{88}Sr, ^{89}Y, ^{95}Mo, ^{111}Cd, ^{139}La, ^{140}Ce, ^{141}Pr, ^{146}Nd, ^{147}Sm, ^{153}Eu, ^{157}Gd, ^{159}Tb, ^{163}Dy, ^{165}Ho, ^{166}Er, ^{169}Tm, ^{172}Yb, ^{175}Lu, ^{232}Th, and ^{238}U were all measured in an Agilent 8800 Triple Quadrupole ICP-MS at the Resnick Water and Environment Lab, California Institute of Technology. Measured isotopes were selected based on the natural abundance of the isotope, the absence of potential ICP-MS interferences given the major elements in the solution (H, N, O, Mg, Ar, and Ca), and the quality of the standard calibration curves. Dwell times were 0.1 s for Mg, Ca, Sc, Mn, Co, Ni, Cu, Zn, Cd, and Fe, and 4 s for all other measured elements. Three replicate scans of each element were collected, each of which consisted of 100 sweeps per replicate. All Mg data was recorded in analog detector mode. Concentrations of other elements were measured in pulse counting mode. Most elements were measured without using a collision cell gas. Ca and Fe were measured using He (4.3 mL/min) as a collision cell gas (He-mode) that 1) improved the quality of the calibration curve for ^{43}Ca and 2) prevented the formation of polyatomic interferences, such as ^{40}Ar^{16}O, for ^{56}Fe. The accuracy and quality of the ^{43}Ca calibration curve in He-mode was consistently superior to that of ^{43}Ca in no-gas mode and ^{44}Ca and ^{46}Ca in either mode. Total sample uptake was less than 4 mL per measurement.

Replicate analyses of the 100x dilution of the standard stock solution were run in intervals (every 8–12 analyses) in every batch as both a quantitative and quick scan (semi-quant mode) standard and used to monitor drift. If drift were to have been detected at >5 % levels (>10 % for He-mode due to the drop in sensitivity), analyses would have been rejected. Note that reduced elemental concentration data for Mg-carbonate sample is derived from ratios of concentrations generated from standard calibration curves (Equation (1)). Relative shifts in concentrations with respect to those of Mg were also monitored to ensure the absence of drift.

Barium forms polyatomic oxides and hydrides that can interfere with REEs (Smirnova et al., 2006). To account for these potential interferences, analysis of 10,000 ppb, 1000 ppb, 100 ppb, and 10 ppb Ba in 5 % nitric solutions, diluted from a MSBA 100 ppm barium solution, was completed. From this analysis, it was demonstrated that interferences at operating conditions described above are negligible at less than about 100 to 10 ppb Ba in solution. Thus, when analyzing samples, ^{137}Ba and Ba/REE ratios were qualitatively monitored in quick scan mode. Ba counts account for <1 % of the count rate of REE analyses and remained well below the analytical precision and accuracy of the REE analyses. The isotopes ^{23}Na, ^{28}Si, ^{31}P, ^{34}S, ^{35}Cl, and ^{39}K were also monitored in quick scan mode to look for other non-carbonate mineral contaminants, such as from water-soluble salts, silicates, and phosphates.

Sample data was blank corrected by subtracting the average procedural blank concentrations in the samples from those of the samples in solution for each element. In addition, elements that were present at concentrations of less than ten standard deviations above the average procedural blank concentrations are considered to occur below the limit of quantification and are thus not reported. Procedural blank corrections were applied to the reported data.

Results were converted to nanograms of element per gram of carbonate (ppb) and weight percent for elements that are traditionally considered major elements in the trigonal carbonate series (Mg, Ca, Fe, and Mn) using Equation (1):

$$[\mathrm{E}_{\mathrm{carbonate}}]\left(\frac{g_{\mathrm{E}}}{g_{\mathrm{carbonate}}}\right)=\frac{[\mathrm{E}_{\mathrm{solution}}]}{[\mathrm{Mg}_{\mathrm{solution}}]+[\mathrm{Ca}_{\mathrm{solution}}]+60.01\left(\frac{[\mathrm{Mg}_{\mathrm{solution}}]}{24.305}+\frac{[\mathrm{Ca}_{\mathrm{solution}}]}{40.078}\right)} \tag{1}$$

which normalizes the concentrations of each element measured in solution to the major cations (only Ca and Mg in this case) and amount of carbonate ion needed to satisfy charge balance. Units of $\mathrm{E}_{\mathrm{carbonate}}$ are grams of the element (g_{E}) per gram carbonate mineral ($g_{\mathrm{carbonate}}$). Equation (1) converts concentrations of element E in solution [$\mathrm{E}_{\mathrm{solution}}$] to concentrations of element in the carbonate [$\mathrm{E}_{\mathrm{carbonate}}$] using concentrations of Mg [$\mathrm{Mg}_{\mathrm{solution}}$] and Ca [$\mathrm{Ca}_{\mathrm{solution}}$] in solution, and molar masses of Ca (40.078 g/mol), Mg (24.305 g/mol), and CO_3 (60.01 g/mol).

2.8. *Matrix matching test*

To test the effects of mismatching the Mg concentration of the matrix, four solutions were produced from the source solutions for the elemental standards, each with the following trace element contents: 500 ppb Ca; 50 ppb Sr; 5 ppb Cd, Co, Cr, Cu, Fe, Mn, Ni, V, and Zn; 0.5 ppb of REEs, Sc, Y, U, and Th; 0.01 ppb Mo. The first solution contained 14,200 ppb Mg, which is equal to half the normal amount of matrix. The second solution contained 28,400 ppb Mg, which is the normal amount of matrix expected for ~5 mg of magnesium carbonate in the sample. The third solution contained 42,600 ppb Mg, which is 50 % more Mg than the normal amount of matrix. The fourth solution contained 56,800 ppb Mg, which is twice the normal amount of Mg used for matrix matching. These solutions were analyzed on the ICP-MS as described above (see Sections 2.6 and 2.7).

2.9. *Recovery test*

To further assess the accuracy of measuring multiple elements in a high Mg matrix, a recovery test was conducted by adding a known mass of each element analyzed (excluding Mg) to solutions derived from magnesite sample M22-224E by the selective digestion protocol described here. A 25 mL split of the solution was poured into a clean DigiTUBE. The solution was spiked with ~300 μL (weighed 0.3036 g) of a concentrated trace element solution derived from the sources of the standard solutions (see Section 2.6). The trace element contributions from this spike propagated to known increases in concentrations of Ca by 98.42 ppb; Sr by 50.16 ppb, REEs, Sc, Y, U, and Th by 0.5016 ppb; Cd, Co, Cr, Cu, Fe, Mn, Ni, V, and Zn by 5.016 ppb; Mo by 0.01003 ppb in the 25.3 mL M22-224E solution. Both the initial and spiked solutions were analyzed on the ICP-MS. The recovery % and spike % are calculated to assess the accuracy of the approach as outlined in Equation 2

$$\text{recovery }\% = 100*\frac{M_{\mathrm{spike}}-M_{\mathrm{initial}}}{K_{\mathrm{spike}}} \tag{2}$$

and Equation 3

$$\text{spike }\% = 100*\frac{K_{\mathrm{spike}}}{K_{\mathrm{spike}}+M_{\mathrm{initial}}} \tag{3}$$

respectively. Here $\mathrm{K}_{\mathrm{spike}}$ is the known increase in concentration of an element resulting from the spike, $\mathrm{M}_{\mathrm{spike}}$ is the measured concentration of an element in the spiked M22-224E solution and $\mathrm{M}_{\mathrm{initial}}$ is the measured concentration of the initial (not spiked) M22-224E solution baseline.

2.10. *Bulk XRF analysis of host sediment samples*

Whole rock major and trace elements in host sediment samples were characterized by x-ray fluorescence (XRF) analysis as described by Bucholz and Spencer (2019). Samples analyzed include K-3.4S, K-7.6S, K-8.8S, K-9.8S, and K-10.8S from the depth transect in the Kunwarara mine.

2.11. *Micro-XRF mapping*

Chemical imaging of thin sections (K-7.6 and K-10.8) was accomplished with a Bruker M4 Tornado benchtop μXRF spectrometer in the Caltech Division of Geological and Planetary Science Analytical Facility. X-rays were generated from a rhodium tube excited to 50 kV with 600 μA current and were focused onto samples with polycapillary optics as samples were rastered beneath the primary X-ray beam. Analyses were performed under vacuum (*ca.* 2 mbar) to maximize sensitivity to Mg and other light elements. Fluorescent X-ray energy spectra were measured simultaneously on two 30 mm^2 silicon drift energy dispersive spectrometer detectors and assigned to 40 μm-wide pixels, which had primary beam dwell times of 5–10 ms per pixel. Bruker software (Bruker M4 Tornado v. 1.6) was used to deconvolve fluorescent X-ray EDS spectra from background, emission line overlaps, and detector artifacts (i.e., pile-up peaks and detector escape peaks).

2.12. *Field emissions scanning electron microscopy*

To identify and capture images of primary and secondary phases in the host sediment samples (K-3.4S, K7.6S, K-8.8S, K-9.8S, and K10.8S), aliquots of consolidated sediment fragments were loaded onto a ZEISS 1550VP Field Emissions Scanning Electron Microscope (FESEM) at

Caltech. The instrument includes an Oxford X-Max SDD X-ray Energy Dispersive Spectrometer (EDS) system, which was used for targeted chemical analysis of mineral grains and coatings for the purpose of mineral identification. The back scatter electron (BSE) detector on the FESEM was used for compositional contrast imaging.

2.13. Powder X-ray diffractometry

Separates of carbonate samples from the Kunwarara depth profile were powdered in an agate mortar and pestle and analyzed in a PANalytica X'Pert Pro Powder Diffractometer with a Cu-kα X-Ray source in the Steele Lab at Caltech. Background baseline and Rachinger corrections for kα-2 peaks were made to the X-Ray Diffraction (XRD) spectra.

3. Results

Major, minor, and trace element concentrations in Mg-carbonates from the Kunwarara mine are presented in Tables 2–4. XRD analyses of powdered carbonate nodules confirmed that the samples from the Kunwarara depth transect consisted of either pure magnesite (K-9.8, K-10.8, and K-11.8) or mixtures of magnesite and dolomite (K-7.6, and K-8.8) for samples collected in the upper most 1.5 m (6.8–9.3 m depth) carbonate-bearing horizon (Figure A1 in Appendix A). Calculated carbonate contents for the ICP-MS analyses were determined by calculating the carbonate masses from the measured Mg^{2+} and Ca^{2+} contents and reporting them as a percentage of the weighed mass of the sample. Calculated carbonate content values are all lower than 100 % for both the heated 5 % nitric digests and the selective digestion method and were typically lower for the selective digestion method than for the nitric digests (Table 2). This could be attributed to a combination of factors: 1) a fraction of the sample solutions was retained in the syringe filters, 2) major insoluble phases were filtered away, and 3) fine particles in suspension were discarded during decanting steps in the selective digestion method. Nonetheless, no relationship between the calculated carbonate content and the Mg-carbonate trace element concentrations for replicate analyses of samples such as K-7.6 is observed. Normalization to carbonate mineral concentrations (Equation (1)) accounts for these factors.

3.1. Precision of the ICP-MS solution measurements and procedural blanks

Precision includes the analytical precision associated with the instrument as well as propagation of procedural blank corrections, which are mostly negligible. Maximum procedural blank masses associated with the selective digestion method span between 100 and 600 ng for Mg, Ca, and Fe, 10–100 ng for Ni and Zn, 1–10 ng for Mn and Cu, and are less than 1 ng for all other elements analyzed (Table A1 in Appendix A). Given 5 mg of digested magnesite, the Mg blank constitutes no more than 0.05 % of the analysis. Likewise, given 5 mg of digested dolomite, the Mg and Ca blanks should account for no more than 0.1 % and 0.06 % of the analyses, respectively.

For REEs and Y, the 1σ precision (relative standard deviation from analyzing a single powder aliquot with blank correction) of the reported concentration is better than 10 %, and it is about 2 % on average. The 1σ precisions of Fe, Cu, V, and U spans from ~2 % to ~10 % of their reported concentration and the 1σ precisions of Mg, Mn, and Sr is better than ~4 %. The precisions of Co and Ni are better than 7 % of their reported concentration and are about 3 % on average. The 1σ precision of Ca and Sc widely spans from ~1 % to ~18 % of their reported concentrations. The precision of Ca improved where Ca transitions from a major element (~10 wt %) to a minor element (<1 wt %). The 1σ precision of Cd span 10–40 % and Th, 1–13 %.

3.2. Recovery and matrix matching tests

Recovery test results are presented in Fig. 4 and Table A.2 in Appendix A. The accuracy of solution concentrations measured by ICP-MS are better than 5 %, except for Fe (~31 %), Zn (~9 %), and Sc (~8 %); most elements are within 1-2σ precision of perfect recovery. Poor

Table 2

Sample names, method, weighed masses, calculated carbonate content, weight percent (wt. %) concentrations of Mg, Ca, Mn, and Fe, and 1σ uncertainties (standard deviation). The numbers or letters in the paratheses following K-7.6 and K-10.8 indicate aliquot numbers and averages between samples processed by the same protocol (av). Rows representing average elemental concentrations of K-7.6 determined by the carbonate mineral selective digestion method and by digestion in heated 5 % nitric acid are reported in bold font. BQL indicates that an analysis was below the limit of quantification. In the Method column, "5 % Nitric" indicates that the sample was processed by a heated 5 % nitric digest while "Hot Acetic" indicates that the sample was processed by the selective digestion method.

Sample	Minerology	Method	Weighed Mass(mg)	Calculated Carbonate Content (%)	Mg (wt. %)	Ca (wt. %)	Mn (wt. %)	Fe (wt. %)
K-7.6 (1)	Mgs + Dol	Hot Acetic	8.3	69	20.11(22)	12.11(15)	0.02103(16)	0.00989(83)
K-7.6 (2)	Mgs + Dol	Hot Acetic	4.9	72	20.61(69)	11.42(52)	0.02076(86)	0.0154(13)
K-7.6 (3)	Mgs + Dol	Hot Acetic	6.5	55	20.12(42)	12.10(62)	0.02090(52)	0.0146(12)
K-7.6 (4)	Mgs + Dol	Hot Acetic	6.4	77	20.99(23)	10.89(26)	0.02078(24)	0.01299(94)
K-7.6 (5)	Mgs + Dol	Hot Acetic	4.8	78	20.67(65)	11.33(26)	0.02053(62)	0.0144(12)
K-7.6 (6)	Mgs + Dol	Hot Acetic	7.4	77	20.87(25)	11.06(32)	0.020753(96)	0.01142(79)
K-7.6 (7)	Mgs + Dol	Hot Acetic	5.1	78	20.91(79)	10.99(28)	0.02094(64)	0.0186(11)
K-7.6 (8)	Mgs + Dol	Hot Acetic	5.2	68	20.48(72)	11.59(22)	0.02107(79)	0.0156(14)
K-7.6 (av)	**Mgs + Dol**	**Hot Acetic**			**20.59(34)**	**11.44(47)**	**0.02085(18)**	**0.0141(27)**
K-7.6 (9)	Mgs + Dol	5 % Nitric	5.1	89	20.74(38)	11.239(78)	0.02138(63)	0.1636(17)
K-7.6 (10)	Mgs + Dol	5 % Nitric	6.5	88	20.737(90)	11.24(29)	0.021090(22)	0.1738(21)
K-7.6 (11)	Mgs + Dol	5 % Nitric	4.8	91	20.64(24)	11.37(65)	0.02097(42)	0.1982(21)
K-7.6 (12)	Mgs + Dol	5 % Nitric	5.7	89	20.66(19)	11.34(52)	0.02096(15)	0.1908(25)
K-7.6 (13)	Mgs + Dol	5 % Nitric	4.7	89	20.86(25)	11.07(57)	0.02099(32)	0.1554(27)
K-7.6 (14)	Mgs + Dol	5 % Nitric	5	86	20.63(44)	11.38(42)	0.02086(23)	0.1758(31)
K-7.6 (15)	Mgs + Dol	5 % Nitric	4.7	88	20.77(54)	11.19(62)	0.02052(68)	0.1636(23)
K-7.6 (16)	Mgs + Dol	5 % Nitric	6.1	87	20.533(26)	11.52(28)	0.02100(11)	0.1524(20)
K-7.6 (av)	**Mgs + Dol**	**5 % Nitric**			**20.70(10)**	**11.29(14)**	**0.02097(24)**	**0.172(16)**
K-9.8	Mgs	Hot Acetic	6.5	90	28.65(42)	0.248(44)	0.01771(19)	BQL
K-10.8 (1)	Mgs	Hot Acetic	5.9	69	28.54(58)	0.400(37)	0.01586(29)	0.00627(48)
K-10.8 (2)	Mgs	Hot Acetic	7.9	65	28.50(24)	0.455(75)	0.015349(97)	0.00447(36)
K-10.8 (3)	Mgs	5 % Nitric	5	77	28.53(14)	0.408(52)	0.015766(96)	0.00989(49)
K-10.8 (4)	Mgs	5 % Nitric	5.2	71	28.55(36)	0.388(18)	0.01555(27)	0.01175(34)
K-11.8	Mgs	Hot Acetic	6.4	80	28.56(21)	0.369(51)	0.01661(14)	BQL

Table 3

Rare earth element concentrations in carbonate samples from the Kunwarara mine in ppb by sample and method. Refer to Table 2 caption for table formatting and descriptive information associated with the values in the rows and columns.

Sample	Method	La	Ce	Pr	Nd	Sm	Eu	Gd	Tb	Dy	Ho	Er	Tm	Yb	Lu
K-7.6 (1)	Hot Acetic	13579(44)	7301(40)	2618(21)	11422(99)	2188(12)	682.9(50)	2733(28)	395.9(36)	2530(15)	565.6(27)	1666.3(67)	218.0(21)	1288.9(94)	189.6(33)
K-7.6 (2)	Hot Acetic	12710(270)	6560(160)	2496(68)	10930(270)	2116(63)	648(16)	2615(42)	379.3(60)	2426(64)	535(13)	1590(58)	209.4(96)	1250(28)	179.7(60)
K-7.6 (3)	Hot Acetic	13600(350)	6990(160)	2697(54)	11860(260)	2333(83)	719(13)	2820(94)	411(13)	2598(92)	571(18)	1672(78)	218.7(42)	1289(55)	182.8(47)
K-7.6 (4)	Hot Acetic	12612(90)	6693(38)	2440(20)	10741(22)	2065(21)	643.6(67)	2583(15)	373.4(48)	2378(21)	530.2(54)	1571(15)	201.2(26)	1212(19)	175.2(22)
K-7.6 (5)	Hot Acetic	12250(340)	6480(220)	2372(83)	10370(290)	2016(30)	624.6(76)	2468(64)	359.6(46)	2322(64)	515(17)	1512(59)	198.2(73)	1170(59)	170.2(23)
K-7.6 (6)	Hot Acetic	12544(95)	6711(44)	2435(18)	10680(100)	2079(17)	640(14)	2559(14)	374.7(20)	2384(31)	531.7(21)	1573(12)	203.9(14)	1212.2(56)	177.5(25)
K-7.6 (7)	Hot Acetic	12740(330)	6770(200)	2468(74)	10820(320)	2109(64)	646(21)	2610(100)	379.2(82)	2406(40)	542(15)	1580(65)	210.1(68)	1222(52)	175.4(71)
K-7.6 (8)	Hot Acetic	13130(220)	6820(120)	2564(60)	11220(310)	2173(53)	681(24)	2663(53)	386.1(85)	2482(76)	554(16)	1637(53)	216.2(30)	1281(17)	184.2(36)
K-7.6 (av)	**Hot Acetic**	**12890(490)**	**6790(260)**	**2510(110)**	**11010(470)**	**2135(98)**	**661(31)**	**2630(110)**	**382(15)**	**2441(90)**	**543(19)**	**1600(54)**	**209.5(78)**	**1241(44)**	**179.3(61)**
K-7.6 (9)	5 % Nitric	12910(260)	7380(140)	2452(46)	10700(180)	2064(38)	640(14)	2535(57)	373.8(29)	2371(63)	528(12)	1558(41)	201.0(73)	1194(36)	174.19(80)
K-7.6 (10)	5 % Nitric	12373.6(29)	7113(12)	2335(10)	10187(64)	1960(21)	604.9(93)	2446(30)	353.7(51)	2285(13)	514.8(48)	1516.7(43)	197.87(88)	1179.0(73)	170.3(40)
K-7.6 (11)	5 % Nitric	12180(190)	7137(96)	2308(41)	10110(150)	1967(66)	611(17)	2450(82)	354.7(90)	2305(26)	515(17)	1523(17)	199.3(24)	1172(25)	173.3(20)
K-7.6 (12)	5 % Nitric	12186(33)	7083(12)	2293(14)	10080(100)	1901(23)	598.7(54)	2425(24)	349.0(38)	2240.9(58)	508.2(51)	1498(16)	193.73(78)	1157.4(68)	169.6(14)
K-7.6 (13)	5 % Nitric	12040(250)	7030(150)	2246(47)	9770(200)	1871(33)	578.5(41)	2330(41)	336.5(53)	2173(36)	491(12)	1456(38)	192.7(65)	1157(27)	168.3(56)
K-7.6 (14)	5 % Nitric	12700(300)	7270(200)	2444(69)	10790(270)	2099(53)	650(20)	2635(64)	380.7(76)	2450(41)	544.3(41)	1623.9(44)	212.2(30)	1245(24)	182.3(40)
K-7.6 (15)	5 % Nitric	11870(260)	6900(140)	2239(40)	9860(170)	1884(43)	587(22)	2382(54)	348(13)	2231(64)	502(13)	1497(43)	197.1(51)	1166(26)	170.4(34)
K-7.6 (16)	5 % Nitric	12368(75)	7019(35)	2353(20)	10305(49)	1970(21)	608.9(15)	2460(35)	357.1(22)	2293(23)	510.7(54)	1511(11)	197.5(29)	1160(22)	173.3(19)
K-7.6 (av)	**5 % Nitric**	**12330(340)**	**7120(150)**	**2334(81)**	**10230(360)**	**1964(82)**	**610(24)**	**2458(93)**	**357(14)**	**2294(86)**	**514(16)**	**1523(50)**	**198.9(60)**	**1179(30)**	**172.7(44)**
K-9.8	Hot Acetic	703.6(60)	1034.1(84)	193.24(39)	1003.3(22)	262.2(18)	94.7(25)	397.0(75)	62.83(40)	408.8(15)	91.1(25)	256.2(49)	33.16(15)	187.4(33)	28.54(84)
K-10.8 (1)	Hot Acetic	463.4(67)	983.7(58)	128.0(15)	631.4(82)	159.1(40)	50.7(36)	208(19)	32.31(76)	216.7(53)	48.1(14)	147.5(48)	18.71(91)	114.8(24)	15.9(12)
K-10.8 (2)	Hot Acetic	445.9(73)	968.5(40)	128.64(52)	629.9(67)	151.4(46)	50.4(11)	216(11)	31.79(83)	212.96(83)	47.0(12)	144.5(52)	19.33(64)	115.6(32)	16.51(81)
K-10.8 (3)	5 % Nitric	468.5(42)	974.8(80)	135.1(26)	656.6(48)	162.9(82)	51.3(23)	211(15)	33.1(13)	222.5(62)	50.8(14)	148.1(40)	20.18(79)	122.1(52)	16.866(89)
K-10.8 (4)	5 % Nitric	448.9(94)	945(14)	128.1(37)	614.2(85)	157.0(99)	50.6(19)	173(13)	31.4(15)	208.1(54)	47.5(10)	138.5(84)	18.71(81)	113.4(27)	16.6(13)
K-11.8	Hot Acetic	406.6(85)	1005.7(91)	132.6(36)	671.2(21)	164.9(12)	55.8(19)	215.9(70)	36.9(12)	262.2(51)	62.2(14)	186.1(19)	24.51(96)	144.2(28)	20.11(28)

Table 4

Trace element concentrations of Sc, V, Cr, Co, Ni, Cu, Zn, Sr, Y, Mo, Cd, Th, and U in ppb and Ce* (unitless) in carbonates from the Kunwarara mine. Refer to Table 2 caption for table formatting and descriptive information associated with the values in the rows and columns.

Sample	Method	Sc	V	Cr	Co	Ni	Cu	Zn	Sr	Y	Mo	Cd	Th	U	Ce*
K-7.6 (1)	Hot Acetic	1532(77)	201(17)	BQL	4994(71)	388800(1300)	3970(150)	BQL	287400(1200)	22369(89)	BQL	61.6(10)	142.7(44)	63.3(38)	0.2786(18)
K-7.6 (2)	Hot Acetic	1520(130)	317(35)	BQL	5250(340)	400000(16000)	BQL	BQL	262600(8900)	21220(550)	BQL	BQL	143.4(44)	58.5(49)	0.2657(78)
K-7.6 (3)	Hot Acetic	1590(110)	305(26)	BQL	5330(160)	393700(9600)	BQL	BQL	277700(6200)	22510(480)	BQL	BQL	152.0(23)	58.1(51)	0.2637(78)
K-7.6 (4)	Hot Acetic	1459(19)	198(20)	BQL	5410(150)	407800(6300)	3230(180)	BQL	266200(3000)	21150(230)	BQL	64.9(76)	139.1(12)	57.8(34)	0.2747(22)
K-7.6 (5)	Hot Acetic	1428(46)	260(26)	BQL	5360(230)	409500(9300)	3330(240)	BQL	257100(4500)	20620(390)	BQL	BQL	137.9(17)	54.5(42)	0.274(11)
K-7.6 (6)	Hot Acetic	1519(75)	168(16)	BQL	5522(32)	403600(2500)	3410(160)	BQL	265200(2400)	21100(210)	BQL	58.6(65)	128.7(20)	57.5(28)	0.2766(24)
K-7.6 (7)	Hot Acetic	1420(160)	244(29)	BQL	5480(330)	408000(13000)	2690(250)	BQL	266700(6800)	21250(520)	BQL	BQL	133.2(94)	58.9(42)	0.2750(97)
K-7.6 (8)	Hot Acetic	1560(18)	284(26)	BQL	5333(93)	394000(13000)	3480(350)	BQL	280000(10000)	21990(690)	BQL	100(38)	147.3(31)	62.5(53)	0.2680(59)
K-7.6 (av)	**Hot Acetic**	**1503(62)**	**247(54)**	**BQL**	**5340(160)**	**400700(7800)**	**BQL**	**BQL**	**270000(10000)**	**21530(680)**	**BQL**	**BQL**	**140.5(75)**	**58.9(28)**	**0.2720(55)**
K-7.6 (9)	5 % Nitric	2198(80)	3227(61)	39400(1300)	6010(140)	439000(12000)	BQL	BQL	290600(6800)	21170(390)	BQL	BQL	186.6(62)	84.4(32)	0.2978(71)
K-7.6 (10)	5 % Nitric	2380(140)	3378(11)	41830(320)	5951(52)	438100(1500)	BQL	BQL	282900(1000)	20540(20)	BQL	BQL	192.0(46)	84.95(67)	0.29995(66)
K-7.6 (11)	5 % Nitric	2186(50)	3142(69)	42790(890)	7050(150)	429700(9600)	10370(660)	37400(2700)	277200(4900)	20060(340)	45.9(56)	145(67)	184.4(39)	96.6(27)	0.3054(55)
K-7.6 (12)	5 % Nitric	2327(38)	3548(41)	44940(520)	6138(88)	437400(3800)	BQL	BQL	280000(1700)	20209(97)	BQL	BQL	183.6(36)	89.0(14)	0.30355(96)
K-7.6 (13)	5 % Nitric	2115(23)	3136(52)	38230(690)	6034(92)	431400(8600)	BQL	BQL	279700(4600)	20180(360)	BQL	71(49)	176.1(61)	84.01(75)	0.3056(79)
K-7.6 (14)	5 % Nitric	2230(110)	3476(64)	42220(980)	5770(120)	424800(8000)	BQL	BQL	287000(4300)	20830(360)	BQL	103(26)	182.8(51)	92.8(47)	0.2967(98)
K-7.6 (15)	5 % Nitric	2222(87)	3160(120)	39900(1400)	5840(230)	429000(12000)	BQL	BQL	273000(8300)	19650(510)	BQL	71(33)	172.2(50)	81.8(10)	0.3033(78)
K-7.6 (16)	5 % Nitric	2178(40)	2944(15)	37320(330)	5771(42)	422600(1500)	BQL	BQL	282440(820)	20534(85)	BQL	BQL	170.7(28)	80.15(85)	0.2953(21)
K-7.6 (av)	**5 % Nitric**	**2229(84)**	**3250(200)**	**40800(2500)**	**6070(420)**	**431500(6300)**	**BQL**	**BQL**	**281600(5500)**	**20400(480)**	**BQL**	**BQL**	**181.1(74)**	**86.7(56)**	**0.3009(40)**
K-9.8	Hot Acetic	363(41)	269.9(54)	BQL	10150(200)	218300(4500)	BQL	BQL	7535(39)	3168(28)	BQL	BQL	2.44(32)	7.75(66)	0.6680(64)
K-10.8 (1)	Hot Acetic	BQL	322(15)	BQL	7250(110)	90600(6200)	BQL	BQL	8310(120)	2025(24)	BQL	BQL	BQL	BQL	0.962(11)
K-10.8 (2)	Hot Acetic	BQL	345.7(62)	BQL	7160(120)	88200(5300)	BQL	BQL	8212(37)	1978(14)	BQL	BQL	BQL	7.22(70)	0.967(10)
K-10.8 (3)	5 % Nitric	BQL	458(14)	BQL	7260(330)	95050(530)	BQL	BQL	8630(150)	2001(13)	BQL	BQL	5.4(12)	BQL	0.927(12)
K-10.8 (4)	5 % Nitric	BQL	585(27)	8000(390)	7090(110)	95900(2400)	BQL	BQL	8690(210)	1942(19)	38.3(46)	BQL	BQL	BQL	0.941(22)
K-11.8	Hot Acetic	232(44)	637(10)	BQL	2720(100)	BQL	BQL	BQL	9142(97)	2250(30)	BQL	BQL	BQL	7.05(63)	1.043(20)

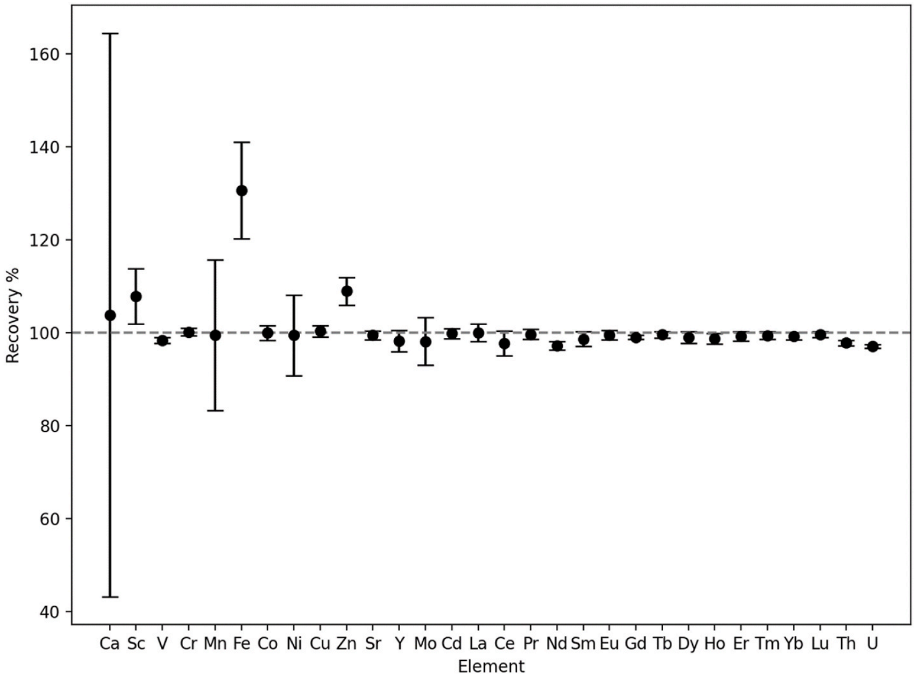

Fig. 4. Recovery % associated with the recovery test as described in Equation (2) plotted by element. The dashed horizontal line indicates perfect recovery. Error bars represent 1σ uncertainties (standard deviation). Data used to generate this figure is available in Table A.2 in Appendix A.

precision while measuring Ca during the recovery test renders the recovery % for Ca ambiguous. The recovery of Fe in He-mode was less accurate than that of other elements and suffered from a high instrument background affecting ~20 ppb solution concentration measurements at the time of the analysis.

The matrix matching evaluation (Fig. 5, Table A.3 in Appendix A) demonstrates that it is possible to accurately measure most major, minor and trace elements in solutions containing Mg concentrations different from those in solution standards. Increasing or decreasing Mg concentrations by a factor of two (28,400 ppb Mg solution) influences concentrations of U, Mo, and Fe by less than 8 %; Th by less than 7 %; Ca, Cr, and Sc by less than 6 %; Cd, Sr, Zn, Co, and V by less than 4 %; Lu, Yb, Tm, Er, Y, Cu, Ni, and Mn by less than 3 %; Ho, Dy, Tb, Gd, Sm, Pr, Ce, and La by less than 2 %; Nd and Eu by less than 1 %. Results indicated

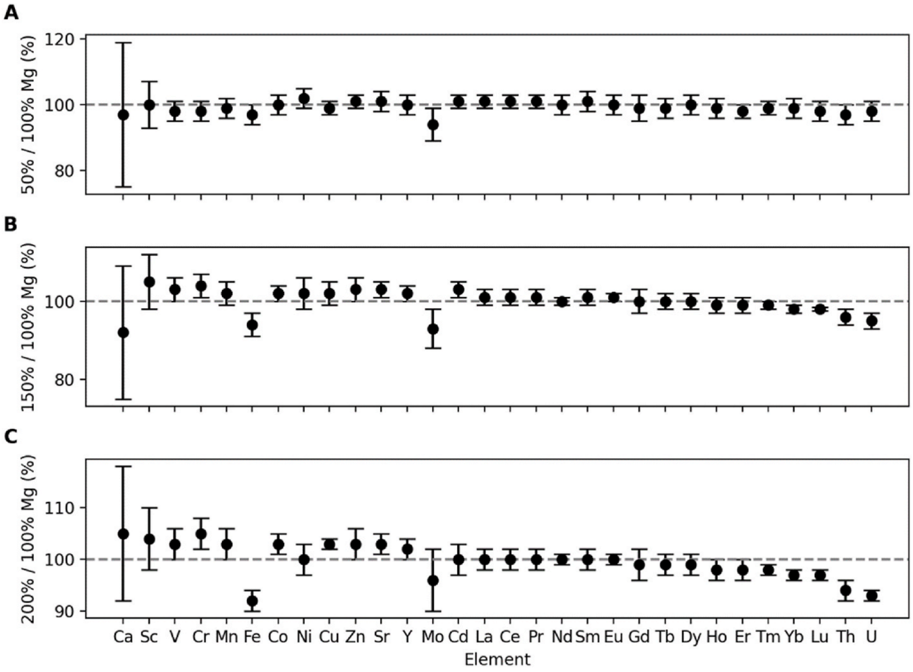

Fig. 5. Matrix matching experiments showing that up to half of the initial sample mass may be non-carbonate phases and still result in accurate analyses. Concentration of the 50 %, 150 % and 200 % Mg matrix solutions are normalized to those of the 100 % Mg matrix solution in panels A (50 %/100 % Mg), B (150 %/100 % Mg), and C (200 %/100 % Mg), respectively. The dashed grey lines indicate where concentrations of the elements in the mismatched matrix (50 %, 150 % and 200 %) and 100 % Mg matrix are the same. Error bars represent 1σ uncertainties (standard deviation). Data used to generate this figure is available in Table A.3 in Appendix A.

that the matrix mismatching will not influence the accuracy of trace element concentrations by more than the measurement precision for net-carbonate-masses of 2.5–10 mg per 50 ml solution, permitting accurate analysis of impure carbonates. All samples reported were within this range (Table 2), indicating that normalizing measured solution concentrations to carbonate mineral concentrations results in accurate data despite minor loss of sample material during ammonium acetate-Milli-Q water cleaning of the samples or digestion of impure powders.

Average trace element concentrations reported for DWA-1 in this study (Table A.4 in Appendix A) are compared to the certificate values provided by Brammer Standards (Table A.5 in Appendix A), which were derived from a compilation of data arranged by Roelandts and Duchesne (1994). In the comparison, average concentrations of Co and Ni determined by ICP-MS reported by Roelandts and Duchesne (1994) were used instead of the proposed values in the certificate of analysis, as there is disagreement between values determined by ICP-MS, NAA, and inductively coupled plasma atomic emission spectroscopy (ICP-AES). All elements evaluated are within 2σ of the certified values except for Ca and Mg, which are both each with 5 % of their recommended concentrations (Fig. 6). Cr quantities yielded from DWA-1 in this study were below the limits of quantification. Cd, Cu, and Mo are not certified.

3.3. Selective digestion of Mg-carbonate

The magnesite + dolomite sample (K-7.6) also contained silicates and iron-manganese oxides (Fig. 1). Powder aliquots of K-7.6 leached and digested in hot acetic acid have less redox sensitive trace elements and derived products than powder aliquots digested in heated 5 % nitric acid. The mean Fe and V concentrations determined by heated 5 % nitric digests are over an order of magnitude higher than those determined by the selective digestion protocol (Fig. 7A).

In comparison to the heated 5 % nitric acid digest, average concentrations of U, Th, and Sc decreased by 22 %, 32 %, and 33 %, respectively, when determined by the selective digestion method; similarly, average Ni and Co decreased by 7 % and 12 %, respectively (Fig. 7A). Average concentrations of Mg, Ca, Mn, and Sr are equal for both digestion protocols. Ce concentrations are systematically lower in the selective digestion than in the heated 5 % nitric acid digestion, whereas those of other REEs and Y appear to be slightly elevated when processed by the selective digestion method (Fig. 7A).

The average Ce anomaly (Ce*) – where Ce* is defined as Ce* = 2 x $Ce_{CI}/(La_{CI} + Pr_{CI})$ – calculated from chondrite normalized (CI) REE concentrations (McDonough and Sun, 1995) is ~10 % lower for the samples processed by the selective digestion method than those digested

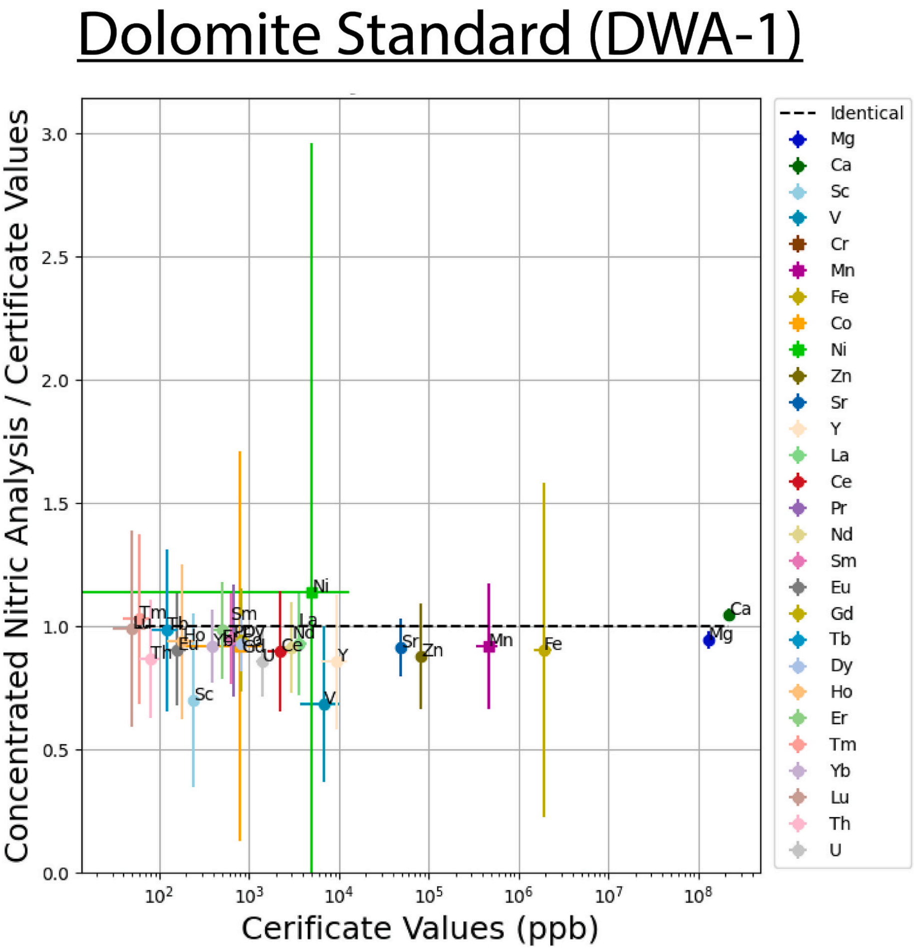

Fig. 6. Certificate and published concentrations (Certificate Values) for elements in DWA-1 (Roelandts and Duchesne, 1994) plotted against average elemental concentrations determined in this study for DWA-1 normalized to Certificate Values (Concentrated Nitric Analysis/Certificate Values). Elements are of Recommended (circles) or Proposed (squares) confidence as tabulated in Table A.5 in Appendix A and presented in the certificate of analysis provided by Brammer Standard. For elements of Proposed confidence (Co and Ni) ICP-MS values reported by Roelandts and Duchesne (1994) are used for normalization instead of proposed values in the certificate. Cr is not shown on this plot because the quantities yielded were below the limits of quantification. Concentrations of Cd, Cu, and Mo are not shown because neither recommended or proposed values are reported in Roelandts and Duchesne (1994). Some of the measured values of these elements are below the limits of quantification for the analyses conducted in this study (Table A.4 in Appendix A). Error bars in this plot represent 2σ uncertainty (~95 % confidence).

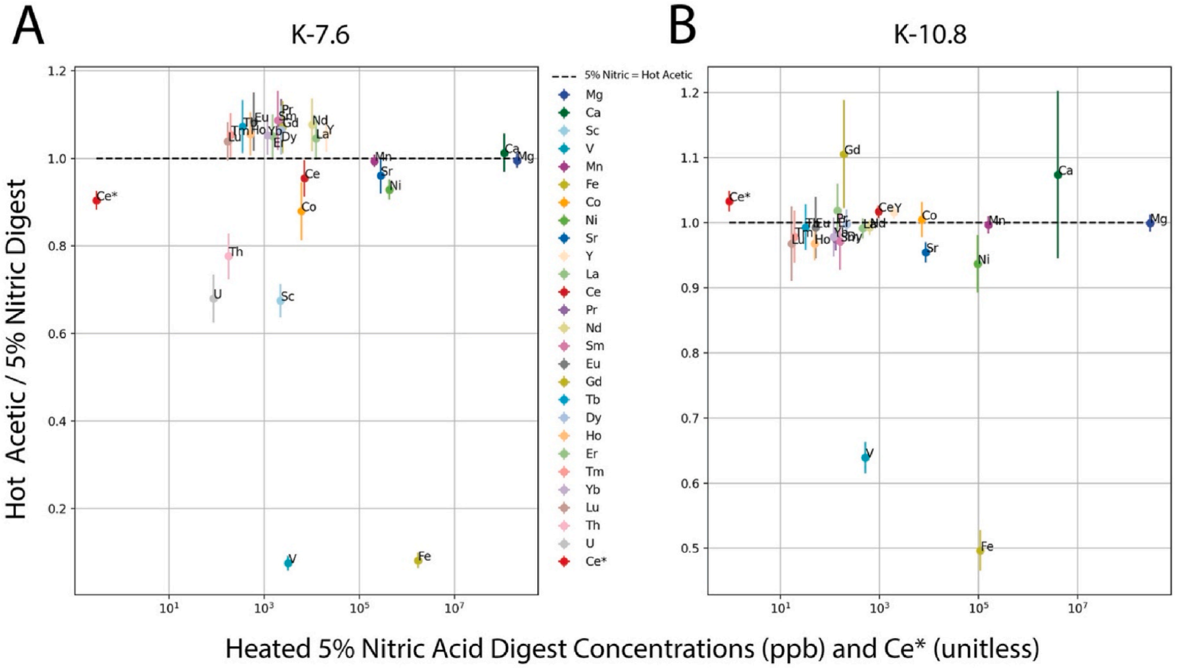

Fig. 7. Average element concentrations and Ce* for K-7.6 and K-10.8 determined by the heated 5 % nitric digest (5 % Nitric) plotted against the element concentrations and Ce* determined by the carbonate mineral selective digestion method (Hot Acetic) normalized to those determined by the 5 % nitric digest. The black dashed line indicates where values determined by the 5 % nitric digest are equivalent those determined by the selective digestion method (5 % Nitric = Hot Acetic). Error bars on panel A represent 1σ uncertainties (standard deviation). Since only two aliquots of K-10.8 were analyzed by both procedures, we plotted the average values and the 1σ precisions added in quadrature and normalized by two to estimate the 1σ uncertainties instead of using the standard deviation calculated from two analyses.

in heated 5 % nitric acid (Fig. 7A–Table 4). Even if alternative expressions for calculating Ce* (e.g., Barrat et al., 2023) are applied, Ce* for the heated 5 % nitric digests remains higher than those resulting from the selective digestion method.

Some redox sensitive elements in the magnesite sample K-10.8, which was mineralogically much purer than K-7.6, were also lower when powder aliquots were leached and dissolved in hot acetic acid rather than heated 5 % nitric acid. Selectively digested aliquots show a ~35 % decrease in the V concentrations and a ~50 % decrease in the Fe concentrations compared to the heated 5 % nitric acid digest (Fig. 7B). Concentrations of other trace elements and Ce* are nearly indistinguishable at 1-2σ uncertainty (Fig. 7B–Tables 2–4). Elements below the limit of quantification (Sc, Cr, Cu, Zn, Mo, Cd, Th, and U) cannot be reliably compared.

3.4. *Reproducibility*

To assess how the external reproducibility associated with the analysis of multiple aliquots of the same powder compares to the internal uncertainty associated with analyzing individual aliquots, we define σ_{internal} as the 1σ standard deviation of the ICP-MS replicate analyses, and σ_{external} as the standard deviation calculated from the determined concentrations of the replicate powder aliquots (Tables 2–4). If the external reproducibility is as expected for a homogeneous powder given the internal uncertainties, then $\sigma_{\text{internal}}/\sigma_{\text{external}} = \text{sqrt}(n_{\text{aliquots}}\text{-}2)/\text{sqrt}(n_{\text{replicates}}\text{-}1) \cong 1.73$ for 8 external aliquots of powder, each measured with three replicates on the ICP-MS. Alternatively, if the external reproducibility is greater (i.e. less reproducible) than expected solely from analytical sources of error, then $\sigma_{\text{internal}}/\sigma_{\text{external}} < 1.73$. If not analytical, a $\sigma_{\text{internal}}/\sigma_{\text{external}} < 1.73$ could be attributed to the heterogeneity in the powders or differences introduced during the dissolution/leaching procedures.

While the internal precision of each element is variable among aliquots, the $\sigma_{\text{internal}}/\sigma_{\text{external}}$ was less than 1.73 for most elements and the Ce* (Figure A.2 in Appendix A), suggesting that even carefully homogenized powders may be heterogeneous or that extraneous sources of error may be introduced when processing replicates. External reproducibility generally improved when employing the selective digestion method compared to the nitric acid digest method, which suggests external variability is related to sample characteristics (e.g., slight inhomogeneity of powder). Fe and V consistently exhibit $\sigma_{\text{internal}}/\sigma_{\text{external}}$ values below one. Fe $\sigma_{\text{internal}}/\sigma_{\text{external}}$ increases from ~0.1 to 0.2 for heated 5 % nitric acid digests to ~0.3–0.5 when processed by the selective digestion method. V $\sigma_{\text{internal}}/\sigma_{\text{external}}$ also tends to improve with the selective digestion method. Methodological distinctions in $\sigma_{\text{internal}}/\sigma_{\text{external}}$ appear for Ca, Co, and U as well (Fig. 7). While $\sigma_{\text{internal}}/\sigma_{\text{external}}$ of some other redox sensitive elements (Ni, Co, Ce, and U) and Sc exhibit scatter around $\sigma_{\text{internal}}/\sigma_{\text{external}} \cong 1.73$ (spanning ~0–2), Sr, Th, and the REEs tend to exhibit $\sigma_{\text{internal}}/\sigma_{\text{external}}$ values < 1. The $\sigma_{\text{internal}}/\sigma_{\text{external}}$ of Mg, Ca, and Mn exhibit a larger range compared to other elements (spanning ~0–5).

3.5. *Kunwarara depth profile*

3.5.1. *Field observations*

The Kunwarara magnesite mine is excavated into unlithified arkosic to sub-arkosic sands. The uppermost 6.8 m of section are comprised of a dark layer of clays underlain by carbonate-free sand and horizons enriched in Fe/Mn-oxyhydroxides. From 6.8 to the bottom of the pit at ~12.3 m, carbonate nodules, pinnacles, and crusts partially replace sand. At shallower horizons, sand grains are partially coated in authigenic clay minerals. The carbonate-bearing sands and the carbonate-free clay-rich sands are separated by a sharp horizontal contact throughout the mine. The upper 1.5 m of the carbonate-bearing section (6.8–8.3 m below the present surface) contains soft, friable, and brittle magnesite ± dolomite nodules with up to decimeter-scale diameters. Dolomite exhibits a greyish color while magnesites are milky white. Dolomite is most common in the upper carbonate-bearing horizons and is absent at depth. Nodules in the upper horizons often include minor detrital silicates, and secondary Fe/Mn-oxide/hydroxide inclusions or stains. Sediments situated in the deepest ~2 m of the pit exposure (10.3–12.3 m) have less clays and almost no secondary oxide phases compared to the shallower sediments. Magnesites hosted deeper in the profile are composed of pure, hard, porcelaneous, cryptocrystalline magnesite nodules and pinnacles that are almost completely free of extraneous mineral inclusions.

3.5.2. Geochemistry of the Kunwarara depth profile

We applied our carbonate mineral-selective digestion method to a suite of samples from the Kunwarara exposure shown in Fig. 2. Major and trace element data for selectively digested Mg-carbonate (by ICP-MS) and host sediment samples (by XRF) are reported in full in Tables 2–4 and Table A.6 in Appendix A and are partially summarized in Fig. 8.

While calcium is a major element in magnesite-dolomite sample K-7.6 (~11.5 wt % Ca), calcium concentrations are less than one weight percent in all other carbonate samples analyzed. Concentrations of Mn and Fe, which occupy octahedral sites in trigonal carbonate minerals, are less than 0.03 wt % in all carbonate samples collected along the sampled transect. Concentrations of Sc, Ni, Sr, Y REEs, Th, and U are much higher in the dolomite-bearing sample (K-7.6) than in the pure magnesite samples analyzed here. In contrast, concentrations of V and Co in K-7.6 are similar to those of pure magnesite samples.

The host sediments sampled along the profile contain detrital quartz, feldspars, and chromite (Fig. 9). Some detrital grains are partially coated with thin films and dense aggregates of phyllosilicates. These phyllosilicates are less prominent but are still present in sample K-10.8S. Host sediments also contain secondary films and nodules of Fe/Mn-oxides/hydroxides, which are absent in K-10.8S but present in all other samples. Sample K-7.6S possesses thin secondary films and specks of cerianite that are sparsely distributed throughout the sediment and are associated with the Mn-oxides/hydroxides and phyllosilicates (Fig. 9B).

Major elements (reported as oxides) in the host sediments include SiO_2 (~56–81 wt %), Al_2O_3 (~5–11 wt %), Fe_2O_3 (~4–15 wt %), MgO (~3–8 wt %), and structural H_2O (~3–9 wt %). Concentrations of Al_2O_3, Fe_2O_3, and structural H_2O are lower by a factor of ~2–3 in K-10.8S compared to all other host sediment samples. Despite the presence of detrital feldspar grains, concentrations of K_2O, Na_2O, and CaO are each less than 1 wt % of the host sediment samples. Trace elements in the host sediments that exhibit the highest concentrations are chromium (~670–4500 ppm) and nickel (~460–2800 ppm), both of which are greater than 2000 ppm in each host sediment sample excluding K-10.8, in which concentrations are below 1000 ppm.

Importantly, we find that carbonate Ce* increases progressively with depth and transitions from <1 to ~1 within the 9.8–10.8 m interval (Fig. 8B–E). This transition corresponds to an order of magnitude decrease in redox sensitive element concentrations from paired host-sediments/samples at the transition between sample K-9.8S and K-10.8 (Fig. 8A). Host sediment sample K-9.8S and those above are rich in interstitial clays between sand grains and Fe/Mn-oxide/hydroxide coatings, while K-10.8S has no Fe/Mn-oxide/hydroxide coatings and only minor clay contents (Fig. 9). Ce concentrations in the paired host sediment samples transition from 39 ± 4 ppm to below detection limit (9.1 ppm) when crossing this depth horizon (Table A.6 in Appendix A).

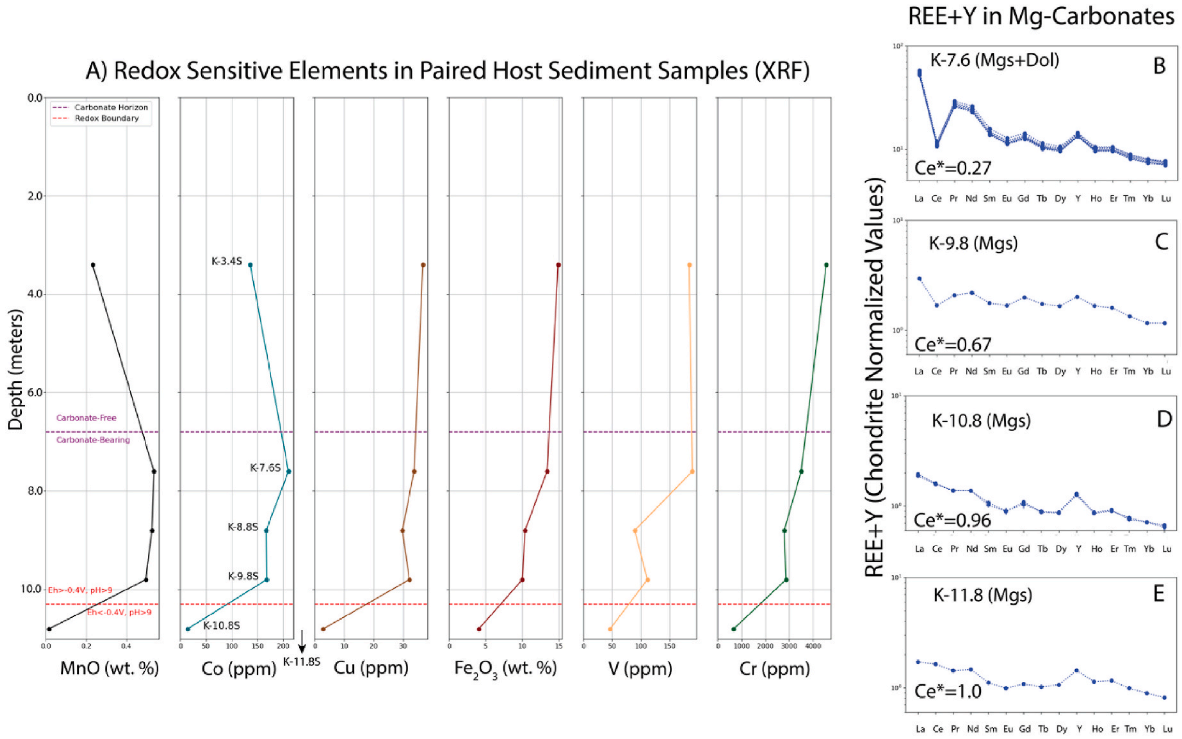

Fig. 8. A summary of geochemical results associated with the depth transect sampled from the Kunwarara pit mine. Panel A includes depth profile plots of the concentrations of redox sensitive elements Mn, Co, Cu, Fe, V, and Cr in the host sediment samples. K-11.8S was not analyzed to fine inseparable carbonate that was well mixed with the sediments, but would plot at 11.8 m depth, and is paired with K-11.8 in panel E. The carbonate horizon and the redox boundary inferred from the data are the purple and red dashed lines in the plots. REE + Y spider diagrams of chondrite normalized (McDonough and Sun, 1995) REE + Y values for carbonate samples K-7.6, K-9.8, K-10.8, and K-11.8 are plotted in Panels B, C, D, and E respectively. Ce* values are reported on each spider diagram. A sharp transition between Ce*<1 and Ce*~1 in the Mg-carbonate is coupled with an order of magnitude drop in the concentrations of redox sensitive elements in the sand samples with depth. This transition occurs between K-9.8S and K-10.8S. Eh-pH conditions (red dashed line in panel A) were estimated from Eh-pH diagrams provided by Brookins (1988). (For interpretation of the references to color in this figure legend, the reader is referred to the Web version of this article.)

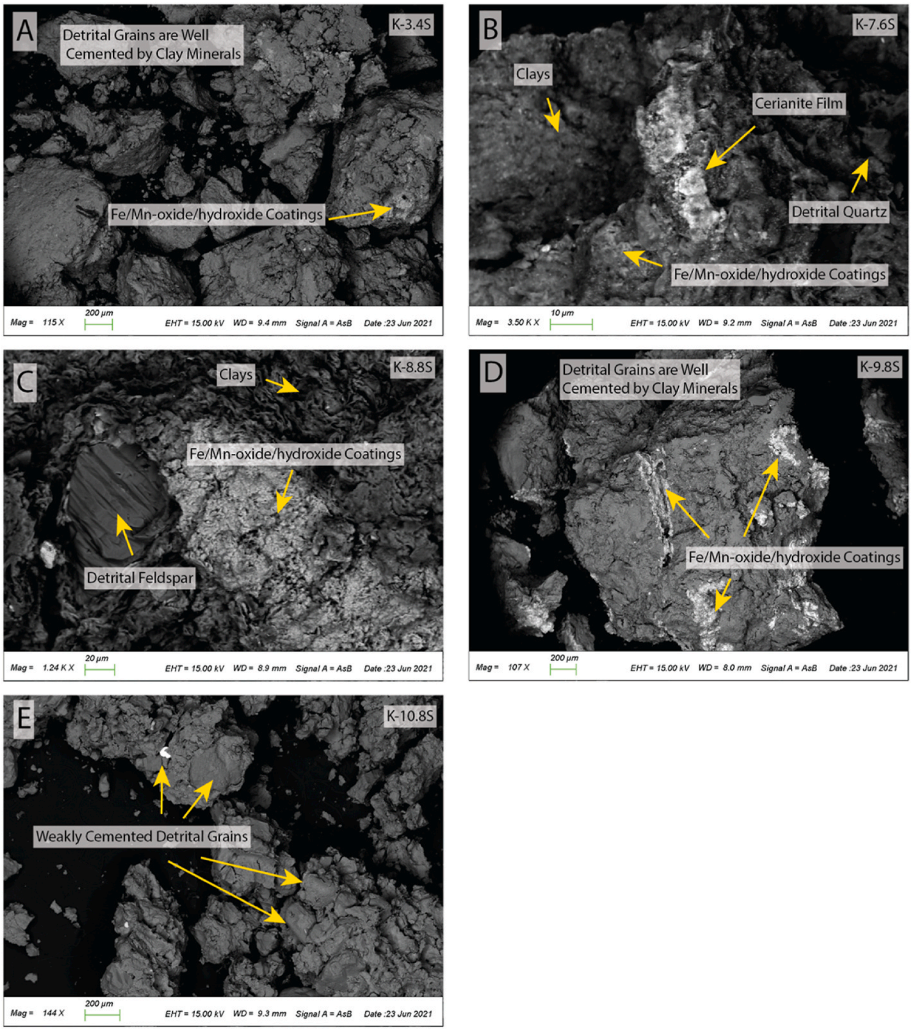

Fig. 9. FESEM BSE compositional contrast images of sand matrix samples along the Kunwarara depth transect. Secondary Fe/Mn/Ce-oxide/hydroxide coatings become absent with depth between samples K-9.8S and K-10.8S.

4. Discussion

4.1. *Efficacy of the selective digestion method*

The precision, accuracy, low detection limits, and small sample size requirements of selective digestions of Mg-carbonates and analysis by solution ICPMS permits investigating the geological and environmental implications of trace element contents in Mg-carbonates. Ce* and some redox-sensitive element (RSE) concentrations derived from samples processed by the selective digestion method are lower than those that experienced the heated 5 % nitric digestion protocol (e.g., sample K-7.6S, Fig. 7A). The lower elemental concentrations result from effective targeting of only the Mg-carbonate phases, minimizing contributions from co-existing Fe/Mn-oxides/hydroxides, silicates, and water-soluble salts. This is particularly important for correctly quantifying Ce* in carbonates because cerium preferentially occurs as Ce^{4+} ions under oxic surface conditions and readily substitutes for Mn^{4+} in the Fe/Mn-oxide/hydroxide structures. Methods that dissolve Fe/Mn-oxides/hydroxides enriched in Ce will result in erroneous Ce* for the hosting carbonates. In our samples, Ce* and Fe concentrations are consistently elevated when processed by the heated 5 % nitric digest as compared to the selective digestion method (Fig. 7A). In contrast, measured Mn contents are indistinguishable between the two methods (Fig. 7). Micro-XRF maps of sample K-7.6 show that while Fe and Mn are both hosted by Fe/Mn-oxides/hydroxides and aluminosilicates, considerable Mn is hosted in the Mg-carbonate itself, which is not the case for Fe (Figure A.3 in Appendix A). From this we infer that, while selective digestion yields most of the Mn from the Mg-carbonate rather than the Fe/Mn-oxides/hydroxides. The oxide minerals may dominate other trace elements in the sample. (Similarly, concentrations of both Fe and Mn in DWA-1 determined by the selective digestion protocol are lower than the certificate values, and lower than concentrations measured in aliquots processed by both the cold concentrated nitric acid and the heated 5 % nitric digestion protocols, which suggests oxide minerals are present in the reference material; Figure A.4, Table A.4, Table A5, and Table A7 in Appendix A).

Measured Fe and V concentrations in sample K-10.8 are also lower when processed by the selective digestion method when compared to the heated 5 % nitric digests, (Fig. 7B), despite the absence of readily observed non-carbonate inclusions in this sample (Fig. 1C and D). We interpret the decrease in Fe and V concentrations to be related to sparsely distributed metal-oxyhydroxides soluble in heated 5 % nitric acid but insoluble by the selective digestion method.

REE concentrations in aliquots of K-7.6 processed by heated 5 % nitric digests are slightly lower than those of the selective digestion method (Fig. 7A), and those of K-10.8 (petrographically pure magnesite) determined by both methods are nearly identical (Fig. 7B). This discrepancy could be explained if a non-carbonate Mg-rich phase in sample K-7.6 with low REE concentrations was digested by the heated 5 % nitric digest, but not by the heated 0.3 M acetic acid. Regardless of its origin, this discrepancy motivates the use of the selective digestion method over other techniques that risk introducing elements from aggressive digestions. Note that REE concentrations for DWA-1 are about 5–10 % lower when processed by the selective digestion method compared to the heated 5 % nitric digest technique (Figure A.4.D, and Table A.7 in Appendix A), suggesting that this response is unique to K-7.6.

Our results show that heated acetic acid digests can produce complete carbonate yields without digesting accessory phases, and that precise and accurate trace element compositions for magnesite ± dolomite samples can be determined from ~2.5 to 10 mg aliquots. Furthermore, ICP-MS measurements require less than 4 ml of the 50 ml solutions produced by our protocols, which permits further significant reduction of both sample mass and solution volume by an order of magnitude (i.e., ~0.5 mg Mg-carbonate aliquots in ~5 ml final solution volumes). A potential limitation is that our method results in simultaneous and complete digestion of both magnesite and dolomite, which may each inherit different trace element characteristics from a fluid (Fernandez-Nieto et al., 2003; Kilias et al., 2006; Lugli et al., 2000). Future development of methods that develop laser ablation ICP-MS techniques or implement step digestions to separately assess the trace element chemistry of dolomite (or other carbonates) and magnesite will be useful. The poor recovery (>5 %) of Fe, Zn, and Sc, and the influences of magnesium matrix matching on the accuracy and precision of Mo (Fig. 5) should be accounted for when interpreting data. Future developments may be necessary to enhance measurement of these elements in magnesite via solution ICP-MS.

4.2. *Pedogenic magnesites capture redox gradients*

Our selective digestion method applied to Mg-carbonates hosted in fluvial sediments sampled along an exposure within the Kunwarara mine shows that the Ce* in magnesite nodules transitions from <1 to ~1 at a depth of ~10.3 m below the present surface (Fig. 8B–E). Importantly, concentrations of RSEs in paired host sediment samples drop by about an order of magnitude in the same horizon (Fig. 9A). This trace elemental change occurs at depths where the Fe/Mn-oxyhydroxides become absent from the host sediments (Fig. 9A–E, Table 1).

We interpret this boundary as a redox front where water-soluble Fe^{2+} and Mn^{2+} ions in the reducing groundwater at depth precipitate as Fe^{3+}, Mn^{3+} and Mn^{4+} oxyhydroxides above the water table. Ce^{4+} preferentially substitutes Mn^{4+} in Fe/Mn-oxide/hydroxides, while other REEs remain in solution in the trivalent state (Brookins, 1988; Laveuf and Cornu, 2009). The preferential scavenging of Ce^{4+} can also be enhanced by adsorption on Fe-oxide/hydroxides (e.g., Ratié et al., 2023) and surface precipitation of cerianite (e.g., Braun et al., 1990) under oxidizing conditions. Thus, under oxidizing conditions the fluids become depleted in Ce^{4+} and carbonates precipitated from these same oxidizing fluids have Ce*<1. In contrast, when carbonates are precipitated under more reducing conditions below the water table, the cerium in solution would be exclusively trivalent and acquire Ce* signatures closer to 1 (unfractionated from the source solution) because, unlike Ce^{4+}, Ce^{3+} is not strongly fractionated away from other trivalent REEs. Importantly, correctly determined REE contents in magnesites can trace transitions between reducing and oxidizing conditions in paleoenvironments.

4.3. *Implications for Mg-carbonates on Earth and Mars*

As demonstrated above, Mg-carbonate phases may have complex formation histories, and these carbonates may occur intermingled with non-carbonate phases (e.g., Clavé et al., 2023; Klein et al., 2022), which is a potential impediment for determining their major and trace element compositions. The method presented here is suited for measuring the elemental composition of magnesite ± dolomite sampled while removing uncertainties associated with the presence of contaminating phases, providing the targeted approach needed for properly constraining environmental conditions controlling the precipitation of Mg-carbonates on Earth and potentially on returned samples from Mars.

The analysis of samples acquired along a depth profile at the Kunwarara mine demonstrates that Ce* in magnesite is a potential marker of changes from reducing to oxidizing conditions as anoxic groundwaters interacted with oxic surficial porewaters. It also permits determining if magnesite precipitation is coeval with or postdates Fe/Mn-oxide/hydroxide precipitation in the transition from reducing to oxidizing conditions. As demonstrated here, our approach is suitable for extracting information from the carbonates themselves, and it avoids the potential pitfalls associated with the coexistence of minerals of distinct origins that are today jointly hosted.

Our results demonstrate that the effective use of Ce* as a redox tracer in magnesite-forming processes requires differentiating the trace element budget of magnesite itself from that of coexisting contaminants near Earth's surface. Similarly, the Ce* of returned Martian Mg-carbonates and the possible co-existence of Mg-carbonates with Fe/Mn-oxyhydroxides in these samples could help place constraints on pH-Eh conditions under which these carbonates formed on Mars as well as in those phases on Earth. As both Mg-carbonates and Fe/Mn-oxide/hydroxides have been positively identified on the surface of Mars and in Martian meteorites (e.g., Ehlmann et al., 2008; Eiler et al., 2002; Farley et al., 2022, 2022; Gattacceca et al., 2014; Lanza et al., 2016; Y. Liu et al., 2021, 2022; Wendt et al., 2011), their trace element contents are directly relevant for unravelling key environmental aspects of Martian evolution. For example, the presence of secondary Fe/Mn-oxides/hydroxides in altered igneous and sedimentary rocks on Mars provides evidence for the existence of both surficial water and an oxidizing Martian atmosphere during the Noachian and the Hesperian (Lanza et al., 2016; Y. Y. Liu et al., 2021; Wendt et al., 2011). While it is uncertain whether this high redox potential resulted from high atmospheric O_2 or halogen cycling in the early Martian atmosphere, Martian Fe/Mn-oxides/hydroxides likely formed in an aqueous environment exposed to the ancient Martian surface (Lanza et al., 2016; Y. Liu et al., 2021; Mandon et al., 2024; Mitra et al., 2023). At times, the ancient Martian atmosphere may have been reducing as a result of volatile input from active volcanism which does not obviously occur on Mars at present (Fanale, 1971; Sholes et al., 2017). Thus, the physical coexistence of Fe/Mn-oxides/hydroxides and Mg-carbonates on the Martian surface would not necessarily indicate coeval formation, as these phases may have formed independently millions or billions of years apart from a combination of deep metasomatic processes, surficial aqueous alteration, and/or evaporative mineralization in a lacustrine environment (Corpolongo et al., 2023; Eiler et al., 2002; Farley et al., 2022; Horgan et al., 2020; Scheller et al., 2022; Simon et al., 2023) though samples could record multiple events if the atmospheric redox potential of early Mars was highly dynamic (Adams et al., 2025).

The Martian meteorite Allan Hills 84001 (ALH84001) contains ~4 billion year old carbonate concretions that record bimodal formation temperatures of ~20 °C in the magnesite-rich concretion rims and ~190 °C in complex calcic magnesio-siderite concretion cores (Borg et al., 1999; Eiler et al., 2002). The ~20 °C formation temperatures of magnesite-rich rims indicate that the magnesites formed near at near-surface conditions in the Martian environment (Eiler et al., 2002). We calculated the Ce anomaly values for Mg-carbonates with <0.10 mol fraction $CaCO_3$ from ALH84001, where La, Ce, and Nd concentrations were previously determined by SIMS (Eiler et al., 2002). The Ce anomaly values vary from 0.45 to 1.01 (Table 5), which indicates that some oxidative scavenging of Ce with respect to other REEs occurred during Mg-carbonate formation on Mars ~4 billion years ago. This scavenging appears to have preferentially occurred in the calcium-poor carbonate concretion cores of ALH84001 with respect to the calcium-poor carbonate rims (Eiler et al., 2002).

On Earth, cerium anomaly values near unity (Ce* = 1) in ancient marine carbonates indicate that the early terrestrial atmosphere of Earth had a low redox potential from ~3.5 billion until the Great Oxidation

Table 5

$CaCO_3$ and REE data for Mg-rich carbonates from Martian meteorite ALH84001 reported by Eiler et al. (2002). While $MgCO_3$, $FeCO_3$, and $MnCO_3$ contents associated with these analyses are not reported, for $CaCO_3$ mole fractions below 0.10 in ALH84001 carbonates, $MgCO_3$, $FeCO_3$, and $MnCO_3$ mole fractions for span 0.56–0.90, 0.08–0.33, and <0.01 respectively (Eiler et al., 2002). Data with a CI subscripts are concentrations normalized to chondrite REE values reported by McDonough and Sun (1995). Ce^*_3 values were calculated using chondrite normalized REEs (La_{CI}, Ce_{CI}, and Nd_{CI}) instead of shale normalized REEs in Equation (3) in Barrat et al. (2023). The "3" subscript in Ce^*_3 is used to indicate that the Ce^*_3 Ce anomaly was calculated differently than Ce* due to the absence of Pr concentrations in Eiler et al. (2002).

$CaCO_3$ (Mole Fraction)	La (ppm)	Ce (ppm)	Nd (ppm)	La_{CI}	Ce_{CI}	Nd_{CI}	Ce^*_3
0.04	0.67	1.54	1.75	2.8	2.51	3.83	0.80
0.05	0.21	0.48	0.41	0.89	0.78	0.90	0.87
0.05	0.41	0.91	0.71	1.7	1.5	1.6	0.90
0.06	1.31	3.20	2.77	5.53	5.22	6.06	0.915
0.07	1.64	4.10	3.15	6.92	6.69	6.89	0.968
0.08	0.87	2.11	1.30	3.67	3.44	2.84	1.01
0.09	0.23	0.53	0.63	0.97	0.86	1.4	0.77
0.09	0.25	0.37	0.81	1.1	0.6	1.8	0.45
0.10	0.39	0.72	0.76	1.6	1.2	1.7	0.73
0.10	0.28	0.49	0.67	1.2	0.80	1.5	0.62
0.12	0.25	0.6	0.44	1.1	0.98	0.96	0.93
0.14	0.27	0.49	0.59	1.1	0.80	1.3	0.69
0.15	0.59	1.71	1.03	2.5	2.79	2.25	1.2
0.22	1.34	3.19	2.65	5.65	5.20	5.80	0.912
0.23	0.98	2.22	1.72	4.1	3.62	3.76	0.91
0.25	0.98	2.32	1.34	4.1	3.78	2.93	1.0
0.44	0.91	1.89	1.45	3.8	3.08	3.17	0.86
0.45	1.33	2.69	1.98	5.61	4.39	4.33	0.847
0.50	0.55	0.89	0.97	2.3	1.5	2.1	0.67
0.54	1.52	2.78	2.33	6.41	4.54	5.1	0.76

Event began ~2.4 billion years ago (X.-M. Liu et al., 2021). From ~2.4 billion years ago to ~0.65 billion years ago, the range of Ce anomalies in marine carbonates progressively expanded to lower values (greater Ce^{4+} fractionation from REE) as the oxidizing potential of Earth atmosphere increased (X.-M. Liu et al., 2021). This comprehensive record demonstrates how Ce* values in the marine carbonates can capture and preserve global environmental conditions for billions of years. Ce anomalies determined in a similar suite of samples from Mars could constrain the evolution ancient redox potential of the Martian atmosphere, addressing questions pertaining to habitability, and the preservation of organics (Broz, 2020; Clark et al., 2021).

When samples are returned from the Mars 2020 Mission, detailed analyses of Ce* in Mg-carbonates separately from coexisting phases could shed light on the influence of redox reactions coincident with carbonate formation near the ancient Martian surface.

5. Conclusion

A carbonate mineral-selective digestion protocol for trace element characterization in Mg-carbonates by solution ICP-MS was developed and evaluated. The efficacy of this method was demonstrated by comparing trace element determinations from the new method to those determined by processing the same samples by a heated 5 % nitric digest. Selective digestion results in lower Ce* and lower concentrations of redox sensitive elements sourced from contaminant phases such as oxides. We applied this new method to magnesite ± dolomite samples from a depth profile in the Kunwarara magnesite mine, in which low Ce* anomalies in the carbonates become absent with depth, coinciding with an order of magnitude drop in redox sensitive element concentrations and absence of secondary Fe/Mn-oxide/hydroxide coatings in paired sand samples. Results demonstrate that selective digestions of magnesite samples can capture redox gradients associated with Fe/Mn-oxide/hydroxide formation and distinguish genetic relationships between the phases from admixture of temporally distinct processes, which may be useful in evaluating returned Mg-carbonates that formed near the Martian surface and may similarly capture environmental conditions associated with carbonate formation.

Funding

This work was supported by Simons Foundation Project Award [668346] and National Science Foundation Graduate Research Fellowship Grant [DGE-1745301].

CRediT authorship contribution statement

Carl Swindle: Writing – review & editing, Writing – original draft, Visualization, Validation, Methodology, Investigation, Funding acquisition, Formal analysis, Data curation, Conceptualization. **Paulo Vasconcelos:** Writing – review & editing, Writing – original draft, Supervision, Resources, Investigation, Conceptualization. **Nathan Dalleska:** Writing – review & editing, Validation, Supervision, Software, Resources, Methodology, Investigation, Data curation. **Emily Cardarelli:** Writing – review & editing, Investigation. **Surjyendu Bhattacharjee:** Writing – review & editing, Investigation. **Zoe Dimarco:** Writing – original draft, Methodology, Investigation. **Kenneth A. Farley:** Writing – review & editing, Visualization, Supervision, Resources, Project administration, Investigation, Funding acquisition, Conceptualization. **Theodore Present:** Writing – review & editing, Writing – original draft, Visualization, Validation, Supervision, Project administration, Methodology, Investigation, Conceptualization.

Declaration of competing interest

The authors declare the following financial interests/personal relationships which may be considered as potential competing interests: Carl Swindle reports financial support was provided by National Science Foundation. Kenneth A. Farley, Carl Swindle, Theodore Present, and Surjyendu Bhattacharjee report financial support was provided by Simons Foundation. If there are other authors, they declare that they have no known competing financial interests or personal relationships that could have appeared to influence the work reported in this paper.

Acknowledgements

We are grateful for support from Mark Liddelow and Qmag for providing access and permission to collect samples to the Kunwarara magnesite mine. We appreciate Peter Martin, Eva Scheller, Kenneth Williford, Kelsey Moore, and Eryn Eitel who participated in collecting samples in the field. We thank the Resnick Institute and the Water and Environment Lab (WEL) at Caltech from providing and maintaining the wet chemistry lab and ICP-MS facilities. We acknowledge Claire Bucholz and Juliet Ryan-Davis for critical assistance conducting whole rock major and trace element analyses of the host sediment samples. We are grateful for the FESEM and micro-XRF mapping facilities at Caltech and assistance from Chi Ma. We are appreciative of feedback received from Paul Asimow, John Eiler, Edward Stolper and Francois Tissot. We appreciate the assistance from Eva Scheller, Benjamin Herren, and those who maintain X-Ray Diffraction facilities in the Steele Lab at Caltech.

Appendix. A Supplementary data

Supplementary data to this article can be found online at https://doi.org/10.1016/j.apgeochem.2025.106494.

Data availability

Data is available in the supporting document (Appendix A).

References

Adams, D., Scheucher, M., Hu, R., Ehlmann, B.L., Thomas, T.B., Wordsworth, R., Scheller, E., Lillis, R., Smith, K., Rauer, H., Yung, Y.L., 2025. Episodic warm climates on early Mars primed by crustal hydration. Nat. Geosci. 18 (2), 133–139. https://doi.org/10.1038/s41561-024-01626-8.

Barrat, J.-A., Bayon, G., Lalonde, S., 2023. Calculation of cerium and lanthanum anomalies in geological and environmental samples. Chem. Geol. 615, 121202. https://doi.org/10.1016/j.chemgeo.2022.121202.

Borg, L.E., Connelly, J.N., Nyquist, L.E., Shih, C.-Y., Wiesmann, H., Reese, Y., 1999. The age of the carbonates in Martian Meteorite ALH84001. Science 286 (5437), 90–94. https://doi.org/10.1126/science.286.5437.90.

Boyle, E.A., 1981. Cadmium, zinc, copper, and barium in Foraminifera tests. Earth Planet Sci. Lett. 53 (1), 11–35. https://doi.org/10.1016/0012-821X(81)90022-4.

Braun, J.-J., Pagel, M., Muller, J.-P., Bilong, P., Michard, A., Guillet, B., 1990. Cerium anomalies in lateritic profiles. Geochem. Cosmochim. Acta 54 (3), 781–795. https://doi.org/10.1016/0016-7037(90)90373-S.

Brookins, D.G., 1988. Eh-pH Diagrams for Geochemistry. Springer Berlin Heidelberg. https://doi.org/10.1007/978-3-642-73093-1.

Brown, A.J., Viviano, C.E., Goudge, T.A., 2020. Olivine-carbonate mineralogy of the jezero Crater region. J. Geophys. Res.: Planets 125 (3). https://doi.org/10.1029/2019JE006011.

Broz, A.P., 2020. Organic matter preservation in ancient soils of Earth and Mars. Life 10 (7), 113. https://doi.org/10.3390/life10070113.

Bucholz, C.E., Spencer, C.J., 2019. Corrigendum to: 'strongly Peraluminous Granites across the Archean–Proterozoic Transition.'. J. Petrol. 60 (9). https://doi.org/10.1093/petrology/egz049, 1851–1851.

Cama, J., Metz, V., Ganor, J., 2002. The effect of pH and temperature on kaolinite dissolution rate under acidic conditions. Geochem. Cosmochim. Acta 66 (22), 3913–3926. https://doi.org/10.1016/S0016-7037(02)00966-3.

Cao, C., Liu, X.-M., Bataille, C.P., Liu, C., 2020. What do Ce anomalies in marine carbonates really mean? A perspective from leaching experiments. Chem. Geol. 532, 119413. https://doi.org/10.1016/j.chemgeo.2019.119413.

Clark, B.C., Kolb, V.M., Steele, A., House, C.H., Lanza, N.L., Gasda, P.J., VanBommel, S. J., Newsom, H.E., Martínez-Frías, J., 2021. Origin of life on Mars: suitability and opportunities. Life 11 (6), 539. https://doi.org/10.3390/life11060539.

Clavé, E., Benzerara, K., Meslin, P.-Y., Forni, O., Royer, C., Mandon, L., Beck, P., Quantin-Nataf, C., Beyssac, O., Cousin, A., Bousquet, B., Wiens, R.C., Maurice, S., Dehouck, E., Schröder, S., Gasnault, O., Mangold, N., Dromart, G., Bosak, T., et al., 2023. Carbonate detection with SuperCam in igneous rocks on the floor of jezero crater, Mars. J. Geophys. Res.: Planets 128 (6), e2022JE007463. https://doi.org/10.1029/2022JE007463.

Corpolongo, A., Jakubek, R.S., Burton, A.S., Brown, A.J., Yanchilina, A., Czaja, A.D., Steele, A., Wogsland, B.V., Lee, C., Flannery, D., Baker, D., Cloutis, E.A., Cardarelli, E., Scheller, E.L., Berger, E.L., McCubbin, F.M., Hollis, J.R., Hickman-Lewis, K., Steadman, K., et al., 2023. SHERLOC raman mineral class detections of the Mars 2020 crater floor campaign. J. Geophys. Res.: Planets 128 (3), e2022JE007455. https://doi.org/10.1029/2022JE007455.

Croudace, I.W., Joron, J.-L., Jaffrezic, H., Meyer, G., Treuil, M., 1982. Neutron activation analysis of seven B.C.S. certified reference materials of geological interest. Geostand. Newsl. 6 (2), 233–239. https://doi.org/10.1111/j.1751-908X.1982.tb00358.x.

Dong, A., Zhu, X.-K., Li, S.-Z., Kendall, B., Wang, Y., Gao, Z., 2016. Genesis of a giant Paleoproterozoic strata-bound magnesite deposit: constraints from Mg isotopes. Precambr. Res. 281, 673–683. https://doi.org/10.1016/j.precamres.2016.06.020.

Ehlmann, B.L., Mustard, J.F., Murchie, S.L., Poulet, F., Bishop, J.L., Brown, A.J., Calvin, W.M., Clark, R.N., Marais, D.J.D., Milliken, R.E., Roach, L.H., Roush, T.L., Swayze, G.A., Wray, J.J., 2008. Orbital identification of carbonate-bearing rocks on Mars. Science 322 (5909), 1828–1832. https://doi.org/10.1126/science.1164759.

Eiler, J.M., Valley, J.W., Graham, C.M., Fournelle, J., 2002. Two populations of carbonate in ALH84001: geochemical evidence for discrimination and genesis. Geochem. Cosmochim. Acta 66 (7), 1285–1303. https://doi.org/10.1016/S0016-7037(01)00847-X.

Fanale, F.P., 1971. History of Martian volatiles: implications for organic synthesis. Icarus 15 (2), 279–303. https://doi.org/10.1016/0019-1035(71)90080-7.

Farley, K.A., Stack, K.M., Shuster, D.L., Horgan, B.H.N., Hurowitz, J.A., Tarnas, J.D., Simon, J.I., Sun, V.Z., Scheller, E.L., Moore, K.R., McLennan, S.M., Vasconcelos, P. M., Wiens, R.C., Treiman, A.H., Mayhew, L.E., Beyssac, O., Kizovski, T.V., Tosca, N. J., Williford, K.H., et al., 2022. Aqueously altered igneous rocks sampled on the floor of Jezero crater, Mars. Science 377 (6614), eabo2196. https://doi.org/10.1126/science.abo2196.

Fernandez-Nieto, C., Torres-Ruiz, J., Subias Perez, I., Fanlo Gonzalez, I., Gonzalez Lopez, J.M., 2003. Genesis of Mg-Fe carbonates from the Sierra Menera magnesite-siderite deposits, Northeast Spain: evidence from fluid inclusions, trace elements, rare Earth elements, and stable isotope data. Econ. Geol. 98 (7), 1413–1426. https://doi.org/10.2113/gsecongeo.98.7.1413.

Gattacceca, J., Rochette, P., Scorzelli, R.B., Munayco, P., Agee, C., Quesnel, Y., Cournède, C., Geissman, J., 2014. Martian meteorites and Martian magnetic anomalies: a new perspective from NWA 7034: martian meteorites & magnetic anomalies. Geophys. Res. Lett. 41 (14), 4859–4864. https://doi.org/10.1002/2014GL060464.

Greenberg, R.R., Bode, P., De Nadai Fernandes, E.A., 2011. Neutron activation analysis: a primary method of measurement. Spectrochim. Acta B Atom Spectrosc. 66 (3–4), 193–241. https://doi.org/10.1016/j.sab.2010.12.011.

Henjes-Kunst, F., Prochaska, W., Niedermayr, A., Sullivan, N., Baxter, E., 2014. Sm–Nd dating of hydrothermal carbonate formation: an example from the Breitenau magnesite deposit (Styria, Austria). Chem. Geol. 387, 184–201. https://doi.org/10.1016/j.chemgeo.2014.07.025.

Horgan, B.H.N., Anderson, R.B., Dromart, G., Amador, E.S., Rice, M.S., 2020. The mineral diversity of Jezero crater: evidence for possible lacustrine carbonates on Mars. Icarus 339, 113526. https://doi.org/10.1016/j.icarus.2019.113526.

Isa, J., Kohl, I.E., Liu, M.-C., Wasson, J.T., Young, E.D., McKeegan, K.D., 2017. Quantification of oxygen isotope SIMS matrix effects in olivine samples: correlation with sputter rate. Chem. Geol. 458, 14–21. https://doi.org/10.1016/j.chemgeo.2017.03.020.

Kilias, S.P., Pozo, M., Bustillo, M., Stamatakis, M.G., Calvo, J.P., 2006. Origin of the Rubian carbonate-hosted magnesite deposit, Galicia, NW Spain: Mineralogical, REE, fluid inclusion and isotope evidence. Miner. Deposita 41 (7), 713–733. https://doi.org/10.1007/s00126-006-0075-5.

Klein, F., Goldsby, D.L., Lin, J., Andreani, M., 2022. Carbonation of serpentinite in creeping faults of California. Geophys. Res. Lett. 49 (15). https://doi.org/10.1029/2022GL099185.

Kuşcu, M., Cengiz, O., Kahya, A., 2017. Trace element contents and C-O isotope geochemistry of the different originated magnesite deposits in Lake District (Southwestern Anatolia), Turkey. Arabian J. Geosci. 10 (15), 339. https://doi.org/10.1007/s12517-017-3102-1.

Lanza, N.L., Wiens, R.C., Arvidson, R.E., Clark, B.C., Fischer, W.W., Gellert, R., Grotzinger, J.P., Hurowitz, J.A., McLennan, S.M., Morris, R.V., Rice, M.S., Bell, J.F., Berger, J.A., Blaney, D.L., Bridges, N.T., Calef, F., Campbell, J.L., Clegg, S.M., Cousin, A., et al., 2016. Oxidation of manganese in an ancient aquifer, Kimberley formation, Gale crater, Mars: manganese fracture fills in Gale Crater. Geophys. Res. Lett. 43 (14), 7398–7407. https://doi.org/10.1002/2016GL069109.

Laveuf, C., Cornu, S., 2009. A review on the potentiality of rare Earth elements to trace pedogenetic processes. Geoderma 154 (1–2), 1–12. https://doi.org/10.1016/j.geoderma.2009.10.002.

Liu, Y.-G., Miah, M.R.U., Schmitt, R.A., 1988. Cerium: a chemical tracer for paleo-oceanic redox conditions. Geochem. Cosmochim. Acta 52 (6), 1361–1371. https://doi.org/10.1016/0016-7037(88)90207-4.

Liu, X.-M., Kah, L.C., Knoll, A.H., Cui, H., Wang, C., Bekker, A., Hazen, R.M., 2021. A persistently low level of atmospheric oxygen in Earth's middle age. Nat. Commun. 12 (1), 351. https://doi.org/10.1038/s41467-020-20484-7.

Liu, Y., Fischer, W.W., Ma, C., Beckett, J.R., Tschauner, O., Guan, Y., Lingappa, U.F., Webb, S.M., Prakapenka, V.B., Lanza, N.L., Agee, C.B., 2021. Manganese oxides in Martian meteorites Northwest Africa (NWA) 7034 and 7533. Icarus 364, 114471. https://doi.org/10.1016/j.icarus.2021.114471.

Liu, Y., Tice, M.M., Schmidt, M.E., Treiman, A.H., Kizovski, T.V., Hurowitz, J.A., Allwood, A.C., Henneke, J., Pedersen, D.A.K., VanBommel, S.J., Jones, M.W.M., Knight, A.L., Orenstein, B.J., Clark, B.C., Elam, W.T., Heirwegh, C.M., Barber, T., Beegle, L.W., Benzerara, K., et al., 2022. An olivine cumulate outcrop on the floor of Jezero crater, Mars. Science 377 (6614), 1513–1519. https://doi.org/10.1126/science.abo2756.

Lu, J., Chen, W., Zhang, W., Liu, H., Simonetti, A., Hu, Z., Liu, Y., Zhao, K., Jiang, S., 2022. Determination of carbon isotopes in carbonates (calcite, dolomite, magnesite, and siderite) by femtosecond laser ablation multi-collector ICP-MS. J. Anal. Atomic Spectrom. 37 (2), 278–288. https://doi.org/10.1039/D1JA00356A.

Lugli, S., Torres-Ruiz, J., Garuti, G., Olmedo, F., 2000. Petrography and geochemistry of the eugui magnesite Deposit(Western pyrenees, Spain): evidence for the development of a PeculiarZebra banding by dolomite replacement. Econ. Geol. 95 (8), 1775–1791. https://doi.org/10.2113/gsecongeo.95.8.1775.

Mandon, L., Ehlmann, B.L., Wiens, R.C., Garczynski, B.J., Horgan, B.H.N., Fouchet, T., Loche, M., Dehouck, E., Gasda, P., Johnson, J.R., Broz, A., Núñez, J.I., Rice, M.S., Vaughan, A., Royer, C., Gómez, F., Annex, A.M., Beyssac, O., Forni, O., et al., 2024. Variable iron mineralogy and redox conditions recorded in ancient rocks measured by in situ Visible/Near-Infrared spectroscopy at jezero Crater, Mars. J. Geophys. Res.: Planets 129 (7), e2023JE008254. https://doi.org/10.1029/2023JE008254.

Marin Carbonne, J., Kiss, A., Bouvier, A.-S., Meibom, A., Baumgartner, L., Bovay, T., Plane, F., Escrig, S., Rubatto, D., 2022. Surface analysis by secondary ion mass spectrometry (SIMS): principles and applications from Swiss laboratories. Chimia 76 (1–2), 26. https://doi.org/10.2533/chimia.2022.26.

McDonough, W.F., Sun, S. -s., 1995. The composition of the Earth. Chem. Geol. 120 (3–4), 223–253. https://doi.org/10.1016/0009-2541(94)00140-4.

Mervine, E.M., Sims, K.W.W., Humphris, S.E., Kelemen, P.B., 2015. Applications and limitations of U–Th disequilibria systematics for determining ages of carbonate alteration minerals in peridotite. Chem. Geol. 412, 151–166. https://doi.org/10.1016/j.chemgeo.2015.07.023.

Milburn, D., Wilcock, S., 1994. The Kunwarara magnesite deposit, central Queensland. In: In Field Conference `94 Capricorn Region. Geological Society of Australia, pp. 99–107.

Milburn, D., Wilcock, S., 1998. Kunwarara Magnesite Depsoit. Geology of Australian and Papua New Guinean Mineral Deposits, pp. 815–818.

Mitra, K., Moreland, E.L., Ledingham, G.J., Catalano, J.G., 2023. Formation of manganese oxides on early Mars due to active halogen cycling. Nat. Geosci. 16 (2), 133–139. https://doi.org/10.1038/s41561-022-01094-y.

Möller, P., 1989. Minor and trace elements in magnesite monograph series on mineral deposits, 28. Gebrüder Borntrager, Berlin-Stutgart, pp. 173–195.

Oskierski, H.C., Bailey, J.G., Kennedy, E.M., Jacobsen, G., Ashley, P.M., Dlugogorski, B. Z., 2013. Formation of weathering-derived magnesite deposits in the New England Orogen, New South Wales, Australia: implications from mineralogy, geochemistry and genesis of the Attunga magnesite deposit. Miner. Deposita 48 (4), 525–541. https://doi.org/10.1007/s00126-012-0440-5.

Pittman, Edward D., 1971. Microporosity in carbonate rocks: geological notes. AAPG (Am. Assoc. Pet. Geol.) Bull. 55 (2). https://doi.org/10.1306/819A3DB2-16C5-11D7-8645000102C1865D.

Pokrovsky, O.S., Golubev, S.V., Schott, J., Castillo, A., 2009. Calcite, dolomite and magnesite dissolution kinetics in aqueous solutions at acid to circumneutral pH, 25 to 150 °C and 1 to 55 atm pCO2: new constraints on CO2 sequestration in sedimentary basins. Chem. Geol. 265 (1–2), 20–32. https://doi.org/10.1016/j.chemgeo.2009.01.013.

Pope, G.J., 2007. *MINERAL DEVELOPMENT LICENCE 196 BOUNDARY FLAT LAGOONS OIL SHALE PROJECT ANNUAL REPORT TO QDME FOR THE PERIOD* (R 3186; Queensland Energy Resources Limited). Queensland Department of Mines and Energy.

Ratié, G., Zhang, K., Iqbal, M., Vantelon, D., Mahé, F., Rivard, C., Komárek, M., Bouhnik-Le Coz, M., Dia, A., Hanna, K., Davranche, M., Marsac, R., 2023. Driving forces of Ce (III) oxidation to Ce(IV) onto goethite. Chem. Geol. 633, 121547. https://doi.org/10.1016/j.chemgeo.2023.121547.

Roelandts, I., Duchesne, J.C., 1994. 1993 compilation of data on five BELGIAN sedimentary rock reference materials: AWI-1, SBO-1, PRI-1, CCH-1 and DWA-1. Geostand. Newsl. 18 (2), 143–184. https://doi.org/10.1111/j.1751-908X.1994.tb00515.x.

Saldi, G.D., Schott, J., Pokrovsky, O.S., Oelkers, E.H., 2010. An experimental study of magnesite dissolution rates at neutral to alkaline conditions and 150 and 200°C as a function of pH, total dissolved carbonate concentration, and chemical affinity. Geochem. Cosmochim. Acta 74 (22), 6344–6356. https://doi.org/10.1016/j.gca.2010.07.012.

Scheller, E.L., Swindle, C., Grotzinger, J., Barnhart, H., Bhattacharjee, S., Ehlmann, B.L., Farley, K., Fischer, W.W., Greenberger, R., Ingalls, M., Martin, P.E., Osorio-Rodriguez, D., Smith, B.P., 2021. Formation of magnesium carbonates on Earth and implications for Mars. J. Geophys. Res.: Planets 126 (7). https://doi.org/10.1029/2021JE006828.

Scheller, E.L., Razzell Hollis, J., Cardarelli, E.L., Steele, A., Beegle, L.W., Bhartia, R., Conrad, P., Uckert, K., Sharma, S., Ehlmann, B.L., Abbey, W.J., Asher, S.A., Benison, K.C., Berger, E.L., Beyssac, O., Bleefeld, B.L., Bosak, T., Brown, A.J., Burton, A.S., et al., 2022. Aqueous alteration processes in Jezero crater, Mars—Implications for organic geochemistry. Science 378 (6624), 1105–1110. https://doi.org/10.1126/science.abo5204.

Searston, S., 1998. *Resource Estimation and the Kunwarara Magnesite Deposit* [Masters Thesis]. University of Tasmania.

Sholes, S.F., Smith, M.L., Claire, M.W., Zahnle, K.J., Catling, D.C., 2017. Anoxic atmospheres on Mars driven by volcanism: implications for past environments and life. Icarus 290, 46–62. https://doi.org/10.1016/j.icarus.2017.02.022.

Simon, J.I., Hickman-Lewis, K., Cohen, B.A., Mayhew, L.E., Shuster, D.L., Debaille, V., Hausrath, E.M., Weiss, B.P., Bosak, T., Zorzano, M.-P., Amundsen, H.E.F., Beegle, L. W., Bell, J.F., Benison, K.C., Berger, E.L., Beyssac, O., Brown, A.J., Calef, F., Casademont, T.M., et al., 2023. Samples collected from the floor of jezero crater with the Mars 2020 perseverance rover. J. Geophys. Res.: Planets 128 (6), e2022JE007474. https://doi.org/10.1029/2022JE007474.

Smirnova, E.V., Mysovskaya, I.N., Lozhkin, V.I., Sandimirova, G.P., Pakhomova, N.N., Smagunova, A.A., 2006. Spectral interferences from polyatomic barium ions in inductively coupled plasma mass spectrometry. J. Appl. Spectrosc. 73 (6), 911–917. https://doi.org/10.1007/s10812-006-0175-0.

Smrzka, D., Zwicker, J., Bach, W., Feng, D., Himmler, T., Chen, D., Peckmann, J., 2019. The behavior of trace elements in seawater, sedimentary pore water, and their incorporation into carbonate minerals: a review. Facies 65 (4), 41. https://doi.org/10.1007/s10347-019-0581-4.

Stack, K.M., Ives, L.R.W., Gupta, S., Lamb, M.P., Tebolt, M., Caravaca, G., Grotzinger, J. P., Russell, P., Shuster, D.L., Williams, A.J., Amundsen, H., Alwmark, S., Annex, A. M., Barnes, R., Bell, J., Beyssac, O., Bosak, T., Crumpler, L.S., Dehouck, E., et al., 2024. Sedimentology and stratigraphy of the shenandoah formation, Western fan, jezero crater, Mars. J. Geophys. Res.: Planets 129 (2), e2023JE008187. https://doi.org/10.1029/2023JE008187.

Tostevin, R., Shields, G.A., Tarbuck, G.M., He, T., Clarkson, M.O., Wood, R.A., 2016. Effective use of cerium anomalies as a redox proxy in carbonate-dominated marine settings. Chem. Geol. 438, 146–162. https://doi.org/10.1016/j.chemgeo.2016.06.027.

Wendt, L., Gross, C., Kneissl, T., Sowe, M., Combe, J.-P., LeDeit, L., McGuire, P.C., Neukum, G., 2011. Sulfates and iron oxides in Ophir Chasma, Mars, based on OMEGA and CRISM observations. Icarus 213 (1), 86–103. https://doi.org/10.1016/j.icarus.2011.02.013.

White, A.F., Peterson, M.L., Hochella, M.F., 1994. Electrochemistry and dissolution kinetics of magnetite and ilmenite. Geochem. Cosmochim. Acta 58 (8), 1859–1875. https://doi.org/10.1016/0016-7037(94)90420-0.

Wilcock, S., 2000. Kunwrara Magnesite Deposit, pp. 129–133.

Yu, J., Day, J., Greaves, M., Elderfield, H., 2005. Determination of multiple element/calcium ratios in foraminiferal calcite by quadrupole ICP-MS: foraminiferal calcite. G-cubed 6 (8). https://doi.org/10.1029/2005GC000964 n/a-n/a.

Zhao, Y., Wei, W., Santosh, M., Hu, J., Wei, H., Yang, J., Liu, S., Zhang, G., Yang, D., Li, S., 2022. A review of retrieving pristine rare earth element signatures from carbonates. Palaeogeogr. Palaeoclimatol. Palaeoecol. 586, 110765. https://doi.org/10.1016/j.palaeo.2021.110765.